Research Square

Preprints are preliminary reports that have not undergone peer review.
They should not be considered conclusive, used to inform clinical practice,
or referenced by the media as validated information.

Quantum squeezing skyrmions

Yunquan Liu

yunquan.liu@pku.edu.cn

Peking University https://orcid.org/0000-0003-1137-7236

zijian lyu

Peking University

Jingze Li

Peking University

Article

Keywords:

Posted Date: November 20th, 2026

DOI: https://doi.org/10.21203/rs.3.rs-11379339/v1

License: This work is licensed under a Creative Commons Attribution 4.0 International License.
Read Full License

Additional Declarations: There is **NO** Competing Interest.

Quantum squeezing skyrmions

Zijian Lyu[1], Jingze Li[1], and Yunquan Liu[1,2,3,*]

[1]State Key Laboratory for Mesoscopic Physics and Frontiers Science Center for Nano-optoelectronics, School of Physics, Peking University, Beijing, 100871, China.
[2]Collaborative Innovation Center of Extreme Optics, Shanxi University, Taiyuan, 030006, China.
[3]Peking University Yangtze Delta Institute of Optoelectronics, Nantong, Jiangsu, 226010, China.
[*]Yunquan.Liu@pku.edu.cn.

Abstract

Skyrmions encode the spatial winding of a vector field into an integer topological charge. Optical skyrmions have been realized predominantly in classical field observables and, more recently, in discrete-variable quantum photonic states. Embedding topology in quantum states offers a route to global quantum observables resilient to local perturbations. Extending this concept to continuous-variable quantum fields would bring topological encoding to bright multimode quantum light, a versatile resource for quantum sensing, imaging and communication. Here we introduce and experimentally realize quantum squeezing skyrmions, a new class of skyrmionic textures whose topology resides in the spatially varying quadrature fluctuations of a two-mode squeezed vacuum state. We generate the state by orbital-angular-momentum-pumped spontaneous parametric down-conversion. We then spatially resolve their covariance using phase-sensitive optical parametric amplification, which maps the local anomalous pair correlation onto the intensity oscillations. This measurement retrieves the local squeezing strength and angle of such quantum topological state. Spatially resolved Wigner-function reconstruction reveals Néel-type, Bloch-type and anti-skyrmion squeezing textures whose topological charge remains stable under propagation and external perturbations. Our results establish entangled quantum fluctuations as carriers of optical topology and provide a route towards topologically structured continuous-variable quantum states.

Introduction

A skyrmion is a continuous vector texture whose spatial winding is quantified by an integer topological charge. Originally proposed as a field-theoretical model of particles and nuclei [1, 2], skyrmions have since emerged as topological textures in chiral magnets [3, 4], liquid crystals [5], and spinor Bose–Einstein condensates [6, 7], among other systems [8, 9]. Because the topological charge is invariant under smooth deformations that preserve the continuity and boundary conditions of the texture [10, 11], skyrmions provide a natural framework for encoding information in global field structure [12–14].

Light offers a versatile platform for constructing skyrmionic textures because its polarization, phase, orbital angular momentum (OAM), and other degrees of freedom can be independently controlled [15]. Optical skyrmion lattices have been realized in evanescent electromagnetic fields through the interference of surface-plasmon modes [16]. Subsequent studies extended optical skyrmions to confined optical fields [17], freely propagating paraxial beams [18], polarization fields in free space [19], three-dimensional particle-like fields [20], momentum-space pseudospin textures [21], spatiotemporal optical wave packets [22], and spin–Poynting dual textures in free space [23]. Across these implementations, the physical vector carrying the skyrmion texture takes different forms, including electric or magnetic fields [16, 17], local optical-spin distributions [23], polarization pseudospins represented by Stokes parameters [18, 19], momentum-space Bloch-mode pseudospins [21], Poynting vectors [23], and spatiotemporal polarization fields [22]. For a broader overview of optical skyrmions, see Ref. [24]. In the particular case of a two-component polarization field described by the field operators $\hat{a}_0(\boldsymbol{r})$ and $\hat{a}_1(\boldsymbol{r})$, the transverse Stokes components are determined by the first-order coherence $C = \langle \hat{a}_0^\dagger \hat{a}_1 \rangle$, and the resulting texture is associated with the compact SU(2) geometry of the Bloch–Poincaré sphere.

Skyrmionic topology has recently been extended into the quantum domain by transferring this compact pseudospin construction to non-local discrete-variable photonic state spaces. In these realizations, the texture is reconstructed from joint Pauli-operator expectation values and is therefore a property of the entangled state [25, 26]. Related work has generalized this approach to high-dimensional entangled OAM states, revealing topology in correlations among spatial-mode subspaces [27, 28]. Besides, local single-photon skyrmions were generated from a solid-state quantum emitter coupled to a spin–orbit-engineered microcavity [29].

Despite these advances, quantum optical skyrmions have so far been formulated in discrete-variable state spaces. Continuous-variable quantum light offers a distinct opportunity in which high photon flux coexists with nonclassical correlations distributed across many optical modes [30, 31]. Such states support parallel measurements and provide scalable resources for quantum sensing, imaging and communication. Extending skyrmionic topology to this regime would combine the global character of topological encoding with the brightness, multimode capacity and parallel readout of continuous-variable quantum systems.

Here we experimentally demonstrate quantum squeezing skyrmions, a new class of continuous-variable skyrmionic textures carried by the spatially structured quadrature fluctuations of a two-mode squeezed vacuum. We generate these states through spontaneous parametric down-conversion pumped by an OAM-carrying beam. This process entangles Gaussian and OAM-carrying spatial modes and transfers the pump's helical phase to their anomalous pair coherence. We organize the local second-order covariance into four real components that reveal two complementary geometries: the non-compact SU(1,1) manifold of two-mode squeezing [32] and a compact three-component texture supporting an S^2-valued skyrmionic mapping. Experimentally, we develop a spatially resolved quantum tomography scheme based on phase-sensitive optical parametric amplification [33–35]. The analyser maps the local anomalous pair coherence onto phase-dependent intensity oscillations recorded with a camera. These measurements reconstruct the quantum covariance of the two-mode squeezed field across the transverse plane. Controlling the winding and offset of squeezing phase produces distinct skyrmionic classes. Their persistence under propagation and external perturbations establishes multimode quantum covariance as a robust platform for topological encoding.

Quantum topology of quadrature fluctuations

Before introducing the quantum squeezing skyrmion, we briefly review, for comparison, the well-established Stokes-vector skyrmions constructed from the first-order coherence between two orthogonal field modes (Fig. 1a) [36]. We consider a representative Gaussian-vortex configuration in which mode 0 has a Gaussian spatial profile and carries zero OAM, whereas mode 1 carries an OAM charge ℓ [37]. Let $\hat{a}_j(\boldsymbol{r})$ denote the local field contribution of mode j, where $\boldsymbol{r} = (r, \varphi)$ specifies the transverse position in polar coordinates. The corresponding local population is $N_j(\boldsymbol{r}) = \left\langle \hat{a}_j^\dagger(\boldsymbol{r}) \hat{a}_j(\boldsymbol{r}) \right\rangle$, $j \in \{0, 1\}$. The local first-order intermodal coherence is $C(\boldsymbol{r}) = \left\langle \hat{a}_0^\dagger(\boldsymbol{r}) \hat{a}_1(\boldsymbol{r}) \right\rangle$. Together with the local population imbalance, its real and imaginary parts define the Stokes vector $\boldsymbol{S}(\boldsymbol{r}) = (2\,\mathrm{Re}\,C(\boldsymbol{r}), 2\,\mathrm{Im}\,C(\boldsymbol{r}), N_0(\boldsymbol{r}) - N_1(\boldsymbol{r}))$. Because mode 1 carries the azimuthal phase $\exp(i\ell\varphi)$. relative to the Gaussian mode, the transverse Stokes components satisfy $S_1(\boldsymbol{r}) + iS_2(\boldsymbol{r}) = 2C(\boldsymbol{r}) \propto e^{i\ell\varphi}$.

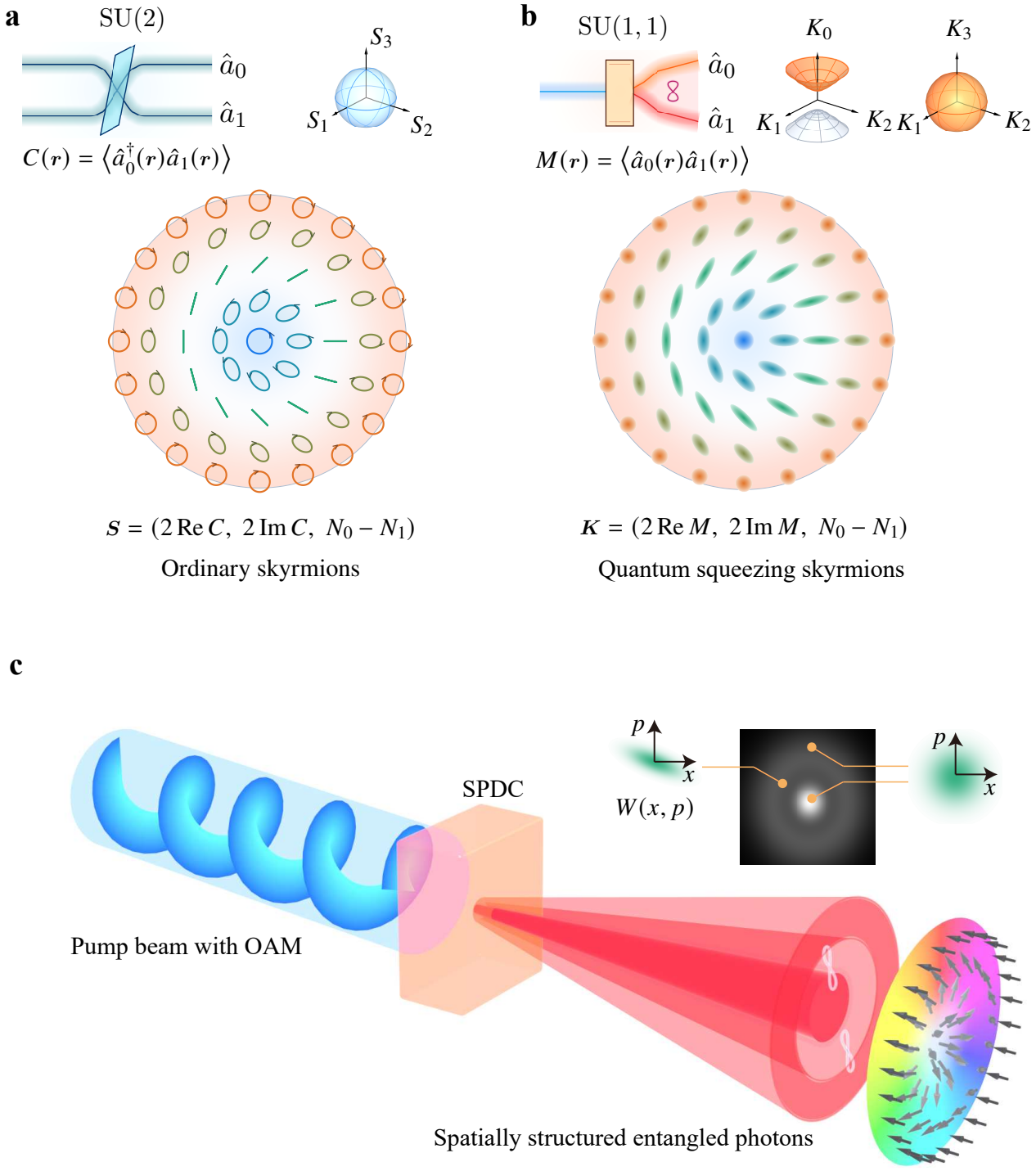


Figure 1. Quantum squeezing skyrmions encoded in spatial covariance. a, Conventional SU(2) Stokes-vector skyrmion constructed from the first-order coherence $C(\boldsymbol{r}) = \langle \hat{a}_0^\dagger(\boldsymbol{r})\hat{a}_1(\boldsymbol{r})\rangle$ between a Gaussian mode and an OAM-carrying mode with $\ell = 1$. Its real and imaginary parts, together with the local population imbalance, define $\boldsymbol{S} = (2\,\mathrm{Re}\,C, 2\,\mathrm{Im}\,C, N_0 - N_1)$. The polarization ellipses visualize the local SU(2) texture. **b**, Quantum squeezing skyrmion constructed from the anomalous pair coherence $M(\boldsymbol{r}) = \langle \hat{a}_0(\boldsymbol{r})\hat{a}_1(\boldsymbol{r})\rangle$. For the representative $\ell = 1$ texture shown, the phase of $M(\boldsymbol{r})$ winds once around the beam axis. The sector (K_0, K_1, K_2) represents the non-compact SU(1,1) geometry of two-mode squeezing, whereas $\boldsymbol{K} = (2\,\mathrm{Re}\,M, 2\,\mathrm{Im}\,M, N_0 - N_1)$ defines the compact covariance texture. The spatially distributed Wigner ellipses show the local squeezing strength and orientation. **c**, Physical realization using frequency-degenerate type-I SPDC. The helical phase of an OAM-carrying pump is transferred to the anomalous coherence of entangled photon pairs occupying the Gaussian and OAM modes, thereby generating the spatial covariance winding. The inset illustrates the spatially resolved phase-space description in terms of local Wigner distribution $W(x, p)$. The phase relation between the Gaussian and OAM-carrying modes sets the squeezing orientation, while their spatial overlap determines the local squeezing strength.

The OAM-dependent phase therefore produces an azimuthal winding of the transverse Stokes vector, while the radial variation of the two modal populations controls the longitudinal component $S_3(\boldsymbol{r}) = N_0(\boldsymbol{r}) - N_1(\boldsymbol{r})$. After normalization, $\boldsymbol{S}(\boldsymbol{r})$ maps the transverse plane onto the Bloch Poincaré sphere, forming the SU(2) Stokes-vector skyrmion visualized by the local polarization ellipses in Fig. 1a.

The situation changes fundamentally when the Gaussian and OAM-carrying modes are coupled through parametric pair creation and become entangled. For the two-mode squeezed vacuum considered here, the first-order coherence vanishes, $C(\boldsymbol{r}) = 0$. However, the two modes exhibit strong phase-sensitive quantum correlations, quantified by the anomalous second-order moment

$$M(\boldsymbol{r}) = \langle a_0(\boldsymbol{r}) a_1(\boldsymbol{r}) \rangle \,. \tag{1}$$

A nonzero $M(\boldsymbol{r})$ correlates the quadrature fluctuations of the two modes, producing a squeezed joint quadrature and an anti-squeezed conjugate quadrature. Consequently, the local uncertainty distribution in phase space becomes an oriented ellipse rather than a circle. The magnitude $|M(\boldsymbol{r})|$ determines the ellipticity of the local Wigner distribution, whereas $\arg M(\boldsymbol{r})$ determines its orientation. The complete covariance-matrix construction and its relation to the local Wigner function are provided in Methods.

To reveal the geometry encoded in these pair correlations, we resolve the complex anomalous coherence into two phase-orthogonal covariance components,

$$K_1(\boldsymbol{r}) = 2\,\mathrm{Re}\, M(\boldsymbol{r}), \qquad K_2(\boldsymbol{r}) = 2\,\mathrm{Im}\, M(\boldsymbol{r}). \tag{2}$$

These components are complemented by the total symmetrized fluctuation $K_0(\boldsymbol{r}) = N_0(\boldsymbol{r}) + N_1(\boldsymbol{r}) + 1$ and the local population imbalance $K_3(\boldsymbol{r}) = N_0(\boldsymbol{r}) - N_1(\boldsymbol{r})$. Together, they define the four-component covariance field $\mathcal{K}(\boldsymbol{r}) = (K_0(\boldsymbol{r}), K_1(\boldsymbol{r}), K_2(\boldsymbol{r}), K_3(\boldsymbol{r}))$. The triplet (K_0, K_1, K_2) constitutes the native SU(1,1) geometry of two-mode squeezing, represented by the hyperboloid in Fig. 1b. To characterize the topology of the spatial covariance pattern, we construct the three-component covariance field

$$\boldsymbol{K}(\boldsymbol{r}) = (K_1(\boldsymbol{r}), K_2(\boldsymbol{r}), K_3(\boldsymbol{r}))\,. \tag{3}$$

For the Gaussian vortex mode pair considered here, the anomalous coherence inherits the helical phase of the OAM-carrying mode. The transverse covariance components therefore satisfy $K_1(\boldsymbol{r}) + iK_2(\boldsymbol{r}) = 2M(\boldsymbol{r}) = 2|M(\boldsymbol{r})|e^{i(\ell\varphi+\varphi_0)}$, where φ_0 is the spatially uniform phase offset. The helical pair phase thus produces an ℓ-fold azimuthal winding of the transverse covariance field. Because a squeezing ellipse is invariant under a rotation by π, the corresponding local squeezing angle is $\theta_{\mathrm{sq}}(\boldsymbol{r}) = \frac{1}{2}\arg M(\boldsymbol{r}) = \frac{\ell\varphi+\varphi_0+\pi}{2} \pmod{\pi}$. The principal axes of the Wigner ellipse therefore rotate at half the rate of the anomalous pair phase. Meanwhile, the radial variation of the two modal populations controls $K_3(\boldsymbol{r}) = N_0(\boldsymbol{r}) - N_1(\boldsymbol{r})$, connecting the two poles of the compact covariance texture. The normalized field $\boldsymbol{n}(\boldsymbol{r}) = \frac{\boldsymbol{K}(\boldsymbol{r})}{|\boldsymbol{K}(\boldsymbol{r})|}$ defines a mapping from the transverse plane onto the unit sphere shown in Fig. 1b. The corresponding topological charge is

$$Q = \frac{1}{4\pi} \int \boldsymbol{n} \cdot (\partial_x \boldsymbol{n} \times \partial_y \boldsymbol{n})\, dx\, dy. \tag{4}$$

This quantity counts the signed number of times the normalized covariance texture covers the unit sphere. This covariance-based topological texture is what we term a *quantum squeezing skyrmion*.

Having established its covariance-based description, we next consider the physical realization of the quantum squeezing skyrmions. In spontaneous parametric down conversion (SPDC), OAM conservation provides a natural mechanism for transferring the spatial phase structure of the pump to photon pairs [38 41]. In the paraxial and rotationally symmetric limit, a pump carrying OAM charge $\ell_p = \ell$ generates signal and idler modes satisfying $\ell_i + \ell_s = \ell$, where ℓ_p, ℓ_s, and ℓ_i denote the OAM charges of the pump, signal and idler fields, respectively. Here we employ frequency-degenerate type-I SPDC, such that the down-converted photons have the same central frequency and polarization and are distinguished only by their spatial modes (Fig. 1c). Within the OAM spectrum, we select the indistinguishable two exchange-related channels $(\ell_s, \ell_i) = (0, \ell)$ and $(\ell_s, \ell_i) = (\ell, 0)$, which together define a two-mode subspace comprising a Gaussian mode and an OAM-carrying mode. In the following, we take $\ell_p = 1$ as a representative case, corresponding to the channels $(0, 1)$ and $(1, 0)$; the construction extends directly to higher-order OAM modes (see Methods). Let a_0 and a_1 denote the annihilation operators of the Gaussian and OAM-carrying modes, respectively. SPDC generates a two-mode squeezed vacuum in this modal basis, $|\Psi\rangle = \exp\left(\xi^* a_0 a_1 - \xi a_0^\dagger a_1^\dagger\right)|0,0\rangle$, where ξ is the complex squeezing parameter. The transverse mode profiles are written as $u_0(\boldsymbol{r}) = A_0(r)$ and $u_1(\boldsymbol{r}) = A_1(r)e^{i(\varphi+\varphi_0)}$. The spatial distribution of this state is

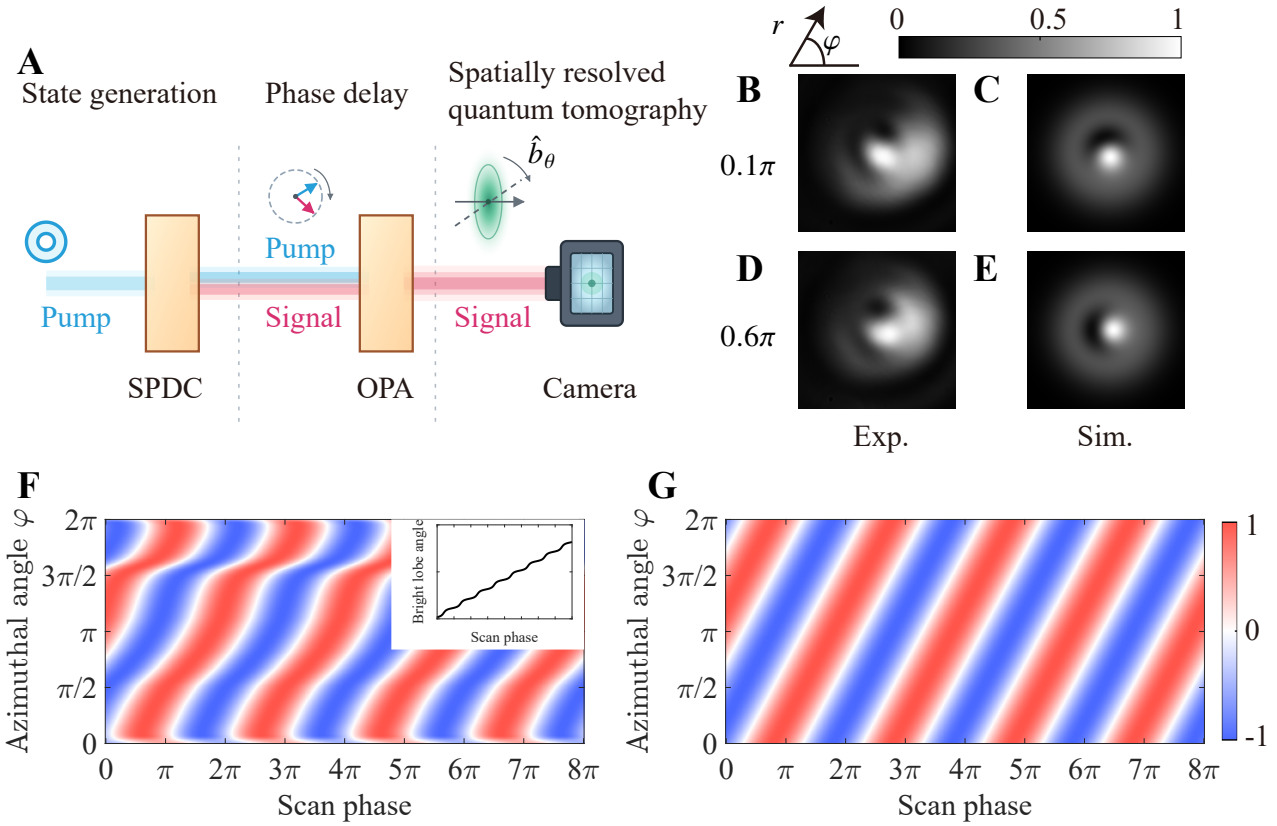


Figure 2. Spatially resolved tomography of the anomalous pair coherence. All measurements and calculations correspond to an OAM pump with $\ell_p = 1$. **a,** Experimental scheme. An OAM-pumped SPDC source generates the spatially structured two-mode squeezed vacuum. A controllable pump-signal phase delay sets the analyser phase δ of the second, phase-sensitive OPA, and the amplified intensity is recorded on a camera. **b-e** Normalized output intensity distributions at $\delta = 0.1\pi$ (**b,c**) and 0.6π (**d,e**). Experimental measurements (**b,d**) agree with the corresponding numerical simulation (**c,e**) and show the phase-dependent rotation of the bright and dark lobes. **f,** Experimental rotation kymograph of the normalized phase-sensitive response $\mathcal{R}(\varphi, \delta)$. The diagonal fringes reveal the azimuthal winding of the anomalous pair phase. Inset, extracted bright-lobe angle versus analyser phase; a linear fit gives a winding number of 1.003. **g,** Theoretical rotation kymograph for a unit-winding pair coherence.

determined by embedding the two modes,

$$b(\boldsymbol{r}) = u_0(\boldsymbol{r})a_0 + u_1(\boldsymbol{r})a_1 \tag{5}$$

Importantly, this Gaussian-vortex superposition provides the spatial scaffold of the quantum squeezing skyrmions. Unlike coherent structured light, however, the two-mode squeezed vacuum has a vanishing mean amplitude, $\langle b(\boldsymbol{r})\rangle = 0$. Its spatial structure is therefore not carried by a classical field amplitude, but by the position-dependent second-order fluctuations of $b(\boldsymbol{r})$. For an ideal two-mode squeezed vacuum, the single-mode anomalous moments vanish $\langle a_0^2\rangle = \langle a_1^2\rangle = 0$. The local phase-sensitive moment can therefore be expressed in terms of the anomalous pair coherence introduced in Eq. (1) as

$$\begin{aligned}\left\langle b^2(\boldsymbol{r})\right\rangle &= 2u_0(\boldsymbol{r})u_1(\boldsymbol{r})\,\langle a_0 a_1\rangle \\ &= 2M(\boldsymbol{r}).\end{aligned} \tag{6}$$

Using the Gaussian and OAM-mode profiles, the anomalous pair coherence takes the explicit spatial form $M(\boldsymbol{r}) = u_0(\boldsymbol{r})u_1(\boldsymbol{r})\,\langle a_0 a_1\rangle \propto A_0(r)A_1(r)e^{i(\varphi+\varphi_0)}$. Its magnitude and phase encode complementary aspects of the local quantum fluctuations. The radial factor $A_0(r)A_1(r)$ sets the strength of the phase-sensitive covariance and is largest where the two spatial modes overlap, whereas the phase $\varphi + \varphi_0$ determines the orientation of the local squeezing quadrature. At each transverse position, the covariance matrix of the two conjugate quadratures of $b(\boldsymbol{r})$ defines a local Gaussian Wigner distribution. Its constant-probability contours are ellipses whose eccentricity reflects the local squeezing strength and whose orientation is fixed by the phase of $M(\boldsymbol{r})$. Where the modal overlap is negligible, the phase-sensitive covariance vanishes and the distribution approaches

rotational symmetry; where the overlap is appreciable, the ellipse becomes increasingly anisotropic. The complete covariance-matrix construction and the reconstruction of the spatially resolved Wigner distributions are described in Methods. Thus, the anomalous pair coherence responsible for two-mode squeezing and entanglement also supplies the spatially winding covariance field from which the quantum squeezing skyrmion is constructed.

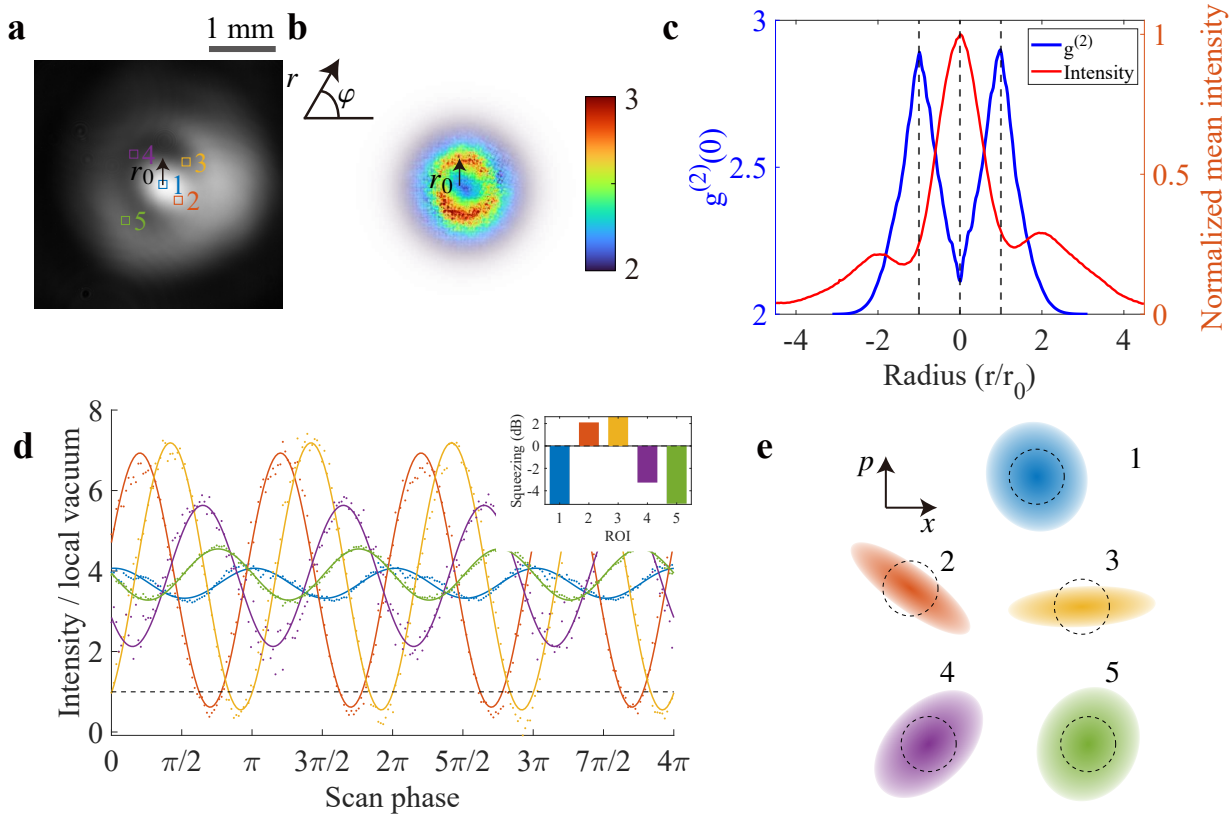


Figure 3. Local covariance and Wigner reconstruction of the squeezing texture . a, Phase-averaged intensity $n_{\mathrm{p}}(\boldsymbol{r})$ and five selected regions of interest (ROIs). ROI 1 is located at the beam centre. From ROI 2 to ROI 5, the radial distance increases uniformly, while the azimuthal angle advances by $\pi/2$ between successive ROIs. **b,** Spatially resolved zero-delay intensity correlation $g^{(2)}(0)$; r_0 denotes the reference radius used to normalize the radial coordinate.**c,** Radial profiles of $g^{(2)}(0)$ (blue) and normalized phase-averaged intensity (red), showing the relation between photon bunching and the spatial mode distribution. **d,** Phase-dependent OPA intensity measured at the five ROIs, each normalized to the corresponding local amplified-vacuum level. Points denote experimental data and solid curves are sinusoidal fits; the dashed horizontal line indicates the vacuum level, measured by filtering out the input signal before the analysing OPA while retaining the pump. Inset, reconstructed quadrature squeezing at each ROI. **e,** Local Wigner ellipses reconstructed from the fitted covariance at the five ROIs. Their eccentricities and orientations represent the local squeezing strengths and angles, respectively; dashed circles indicate the vacuum reference.

Spatially resolved tomography of quantum squeezing skyrmions

To experimentally characterize this new class of quantum squeezing skyrmions, we developed a spatially resolved quantum-tomography scheme based on phase-sensitive optical parametric amplification (OPA) (Fig. 2a). The quantum squeezing-skyrmion state generated by the first parametric interaction serves as the input to a second amplifier, whose pump phase δ is scanned relative to the input squeezing angle. The OPA acts as a phase-sensitive analyzer: it amplifies one joint quadrature while deamplifying the orthogonal one, thereby converting otherwise inaccessible anomalous correlation into a directly measurable intensity response. The resulting intensity is recorded on a camera, providing a parallel readout of these correlations across the entire transverse plane.

For an OPA gain G_2, the spatially resolved transformation can be written as

$$b_{\mathrm{out}}(\boldsymbol{r}) = \cosh G_2\, b_{\mathrm{in}}(\boldsymbol{r}) + e^{i\delta} \sinh G_2\, b^{\dagger}_{\mathrm{in}}(\boldsymbol{r}). \tag{7}$$

The phase-conjugated contribution interferes with the incident field, making the output intensity sensitive to the relative phase between the OPA pump and the anomalous coherence $M(\boldsymbol{r})$. Summing the photon number densities of the amplified Gaussian and OAM spatial-mode components gives,

$$n_{\mathrm{tot}}(\boldsymbol{r};\delta) = n_{\mathrm{p}}(\boldsymbol{r}) + \sinh(2G_2)\left[K_1(\boldsymbol{r})\cos\delta + K_2(\boldsymbol{r})\sin\delta\right], \tag{8}$$

where the phase-insensitive contribution is $n_{\mathrm{p}}(\boldsymbol{r}) = \left[N_0\cosh^2 G_2 + (N_0+1)\sinh^2 G_2\right]|u_0(\boldsymbol{r})|^2 + \left[N_1\cosh^2 G_2 + (N_1+1)\sinh^2 G_2\right]|u_1(\boldsymbol{r})|^2$. Experimentally, this part can be obtained by averaging the measured intensity over the analyser phase. Fig. 2b-e show the measured and calculated output intensity distributions at two representative analyser phases, $\delta = 0.1\pi$ and 0.6π. Changing δ rotates the bright and dark lobes because the OPA selectively amplifies regions whose local pair phase is matched to the pump phase, while deamplifying regions with the opposite phase.

To characterize the rotation of the phase-sensitive intensity pattern, we subtract the phase averaged background and radially average the remaining signal. The resulting response is $\Delta J(\varphi,\delta) = \sinh(2G_2)\left[\overline{K}_1(\varphi)\cos\delta + \overline{K}_2(\varphi)\sin\delta\right] = A(\varphi)\cos[\delta - \delta_M(\varphi)]$, where $A(\varphi) = \sinh(2G_2)\sqrt{\overline{K}_1^2(\varphi) + \overline{K}_2^2(\varphi)}$and $\delta_M(\varphi) = \mathrm{atan2}\left[\overline{K}_2(\varphi), \overline{K}_1(\varphi)\right]$. The amplitude $A(\varphi)$ measures the azimuthally resolved covariance magnitude, whereas $\delta_M(\varphi)$ gives the local pair phase. Normalizing by the oscillation amplitude isolates the latter, $\mathcal{R}(\varphi,\delta) = \frac{\Delta J(\varphi,\delta)}{A(\varphi)} = \cos[\delta - \delta_M(\varphi)]$. The resulting rotation kymograph therefore directly visualizes the azimuthal evolution of the pair phase. For the $\ell_p = 1$ state considered here, $\delta_M(\varphi) = \varphi + \varphi_0$, so the response follows $\varphi = \delta - \varphi_0 \pmod{2\pi}$. The linear relation produces the diagonal bands observed experimentally in Fig. 2f. Their slope reveals the magnitude and handedness of the phase winding. The inset tracks the corresponding rotation of the bright lobe with analyser phase. A linear fit yields a winding number of 1.003, in close agreement with the ideal value of unity. The small variations in the local slope are attributed to spatial walk-off in the nonlinear crystal (see Supplementary Information). Overall, the experimental kymograph closely reproduces the theoretical results in Fig. 2g, confirming a single azimuthal winding of the anomalous pair coherence.

Having established the global phase winding, we next characterize the local quantum fluctuations from which it is formed. Five representative regions were selected from the phase-averaged intensity distribution $n_{\mathrm{p}}(\boldsymbol{r})$(Fig. 3a). The spatial map of the zero-delay correlation $g^{(2)}(0)$ is shown in Fig. 3b. In the bright limit ($N \gg 1$), the spatially structured two-mode squeezed vacuum considered here satisfies,

$$g^{(2)}(\boldsymbol{r};0) = 2 + \frac{4|u_0(\boldsymbol{r})|^2|u_1(\boldsymbol{r})|^2}{\left[|u_0(\boldsymbol{r})|^2 + |u_1(\boldsymbol{r})|^2\right]^2}. \tag{9}$$

This equation shows that $g^{(2)}(\boldsymbol{r};0)$ approaches the thermal value of 2 when the local field is dominated by either spatial mode, and rises towards 3 when the Gaussian and OAM modes contributions become comparable. This behavior is evident in the radial profile in Fig. 3c. Near the beam center, the Gaussian component dominates and the mean intensity is maximal, while $g^{(2)}$ remains close to 2. Moving away from the center, the increasing OAM contribution produces two symmetric bunching peaks along the radial cut, marking the annular region of strongest modal overlap and the largest relative contribution from the anomalous pair coherence. At still larger radii, the OAM component becomes dominant, causing $g^{(2)}$ to return towards 2.

Fig. 3d shows the phase-dependent OPA signals measured at the five selected regions in the beam profile. The oscillations are weak where either mode dominates and strongest in the modal-overlap region, consistent with radial dependence of the anomalous coherence. Fitting their amplitudes and phases determines the local covariance magnitude and squeezing angle, respectively. The corresponding Wigner ellipses are reconstructed in Fig. 3e. Their eccentricities quantify the local squeezing strength, while their orientations track the spatial variation of the squeezing angle. These measurements provide the covariance information required to reconstruct the complete quantum squeezing-skyrmion texture.

Controlled texture and topological robustness

Having established spatially resolved covariance tomography, we next generate and characterize different classes of quantum squeezing skyrmions. Skyrmionic textures are characterized not only by their topological charge, but also by the helicity and handedness of the transverse vector winding. Néel- and Bloch-type skyrmions share the same radial polarity and winding number but differ in helicity. Their transverse components point predominantly along the radial and azimuthal directions, respectively. Anti-skyrmions instead exhibit the opposite azimuthal winding.

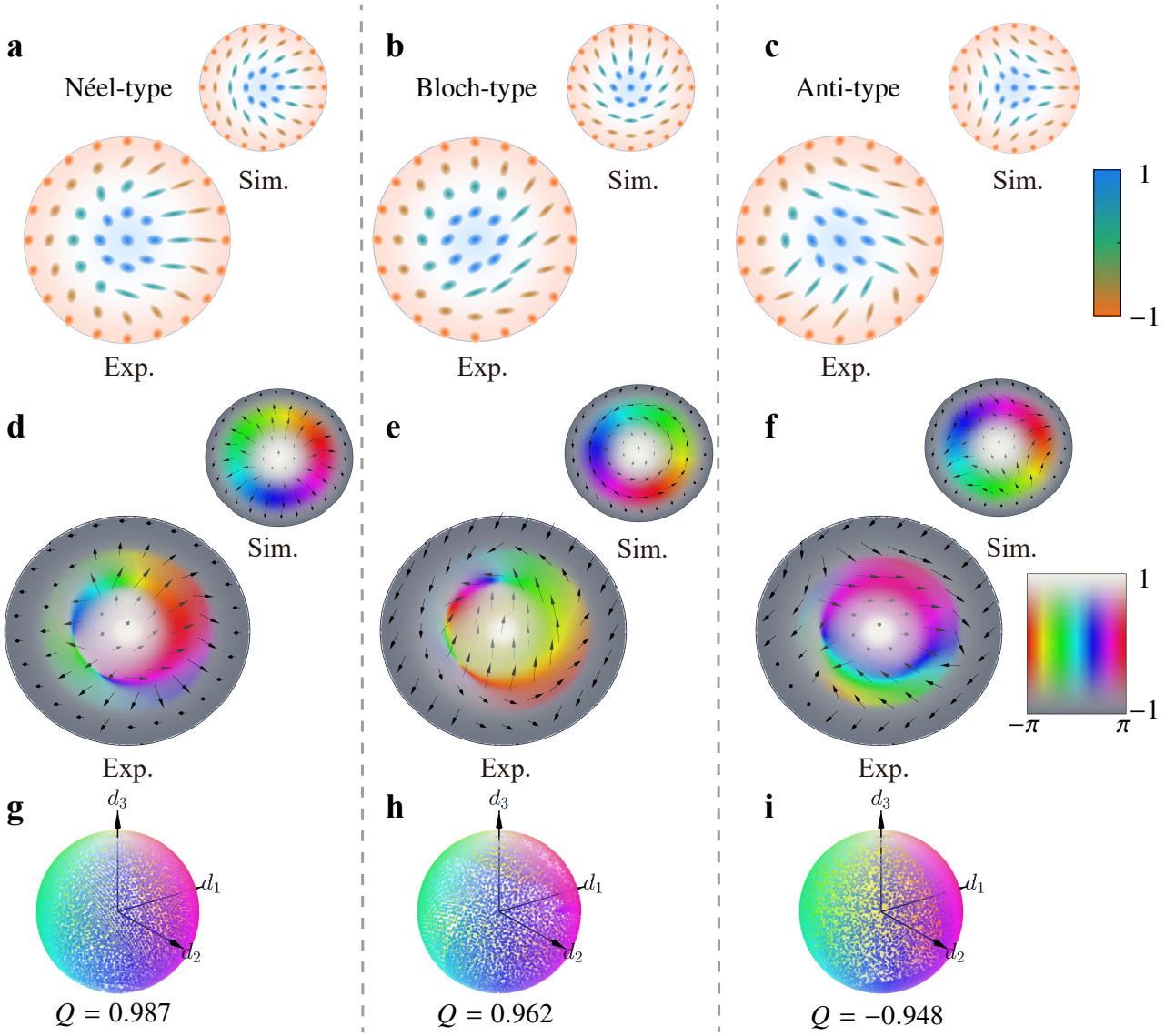


Figure 4. Controlled quantum squeezing-skyrmion textures a-c, Experimentally reconstructed spatial distributions of the local Wigner ellipses for Néel-type (**a**), Bloch-type (**b**) and anti-skyrmionic (**c**) squeezing textures. Insets show the corresponding simulations. The ellipse eccentricity and orientation represent the local squeezing strength and angle, respectively. **d-f,** Normalized covariance-vector fields $\boldsymbol{n}(\boldsymbol{r})$ reconstructed for the Néel-type (**d**), Bloch-type (**e**) and anti-skyrmionic (**f**) states; insets show the theoretical textures. The Néel and Bloch textures are obtained by changing the uniform pair-phase offset φ_0, whereas reversing the OAM winding produces the anti-skyrmions. **g-i,** Corresponding mappings of the experimentally reconstructed normalized covariance vectors onto the unit sphere for the Neél-type (g), Bloch-type (h) and anti-skyrmion (i) textures. The extracted topological charges are $Q = 0.987$, 0.962 and -0.948, confirming unit-magnitude sphere covering and the opposite winding of the anti-skyrmion.

In the covariance construction, these degrees of freedom are encoded in the phase of the anomalous coherence,

$$K_1(\boldsymbol{r}) + iK_2(\boldsymbol{r}) = 2|M(\boldsymbol{r})|e^{i(\ell\varphi+\varphi_0)}. \tag{10}$$

The uniform phase offset φ_0 controls the helicity by rotating the transverse covariance vector throughout the beam, without changing its radial profile or topological charge. For $\ell = 1$, $\varphi_0 = 0$ produces a radial Néel-type texture, whereas $\varphi_0 = \pi/2$ produces an azimuthal Bloch-type texture. Reversing the OAM winding, $\ell \to -\ell$, reverses the handedness and generates an anti-skyrmion. Experimentally, we tune the uniform phase offset by rotating the spiral phase plate about the optical axis, while reversing the plate front-to-back changes the sign of the OAM winding. These operations independently control the helicity and handedness of the squeezing texture.

Figure 4a-c show the reconstructed Wigner-ellipse distributions of the Néel-type, Bloch-type and anti-skyrmionic state, together with their theoretical results. Although their radial squeezing-strength distributions remain similar, their ellipse orientations form distinct spatial patterns. The corresponding normalized covariance-vector fields in Figs. 4d-f reveal the radial, azimuthal and oppositely winding textures, respectively. Mapping

these vectors on to the Poincaré sphere (Figs. 4g-i) shows that each texture covers the sphere once, demonstrating a unit-magnitude topological charge while clearly distinguishing their helicity and handedness.

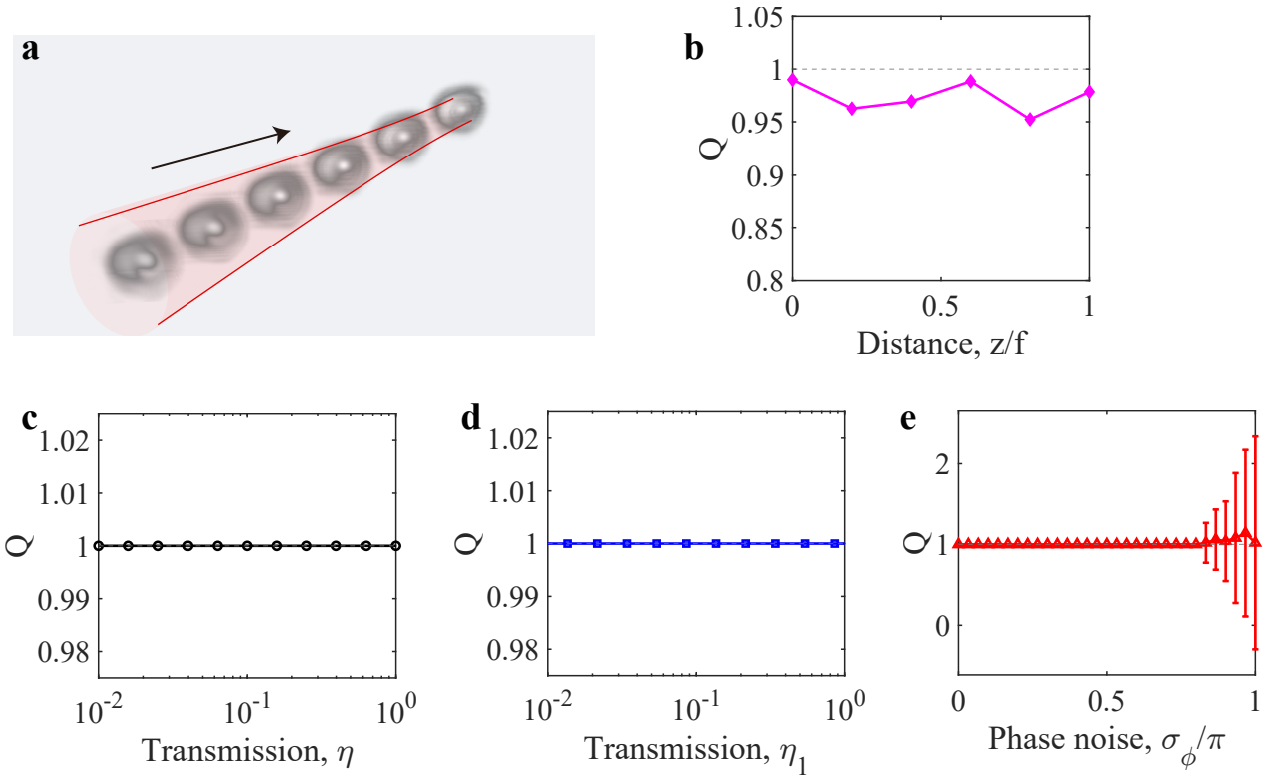


Figure 5. Robustness of quantum squeezing-skyrmion topology a, Experimental phase-averaged intensity distributions $n_{\mathrm{p}}(\boldsymbol{r}; z)$ recorded during propagation towards the focal plane, showing the spatial evolution and focusing of the beam; z/f denotes the propagation distance normalized by the focal length $f = 500$ mm. **b,** Experimental topological charge Q reconstructed at the corresponding propagation distances; the dashed line indicates the ideal unit charge. **c,** Numerically calculated Q under uniform attenuation with transmission η. **d,** Numerically calculated Q under selective attenuation of the OAM mode with transmission η_1. **e,** Numerically calculated Q under spatial phase noise of strength σ_ϕ/π. Symbols show the ensemble mean and error bars indicate the spread over noise realizations.

A defining property of skyrmionic topology is the invariance of its charge under continuous deformations that preserve the continuity and boundary condition of the texture. We test this property for quantum squeezing skyrmions under propagation and external perturbation (Fig.5). We first track the texture as the beam propagates towards the focal plane (Fig. 5a). Focusing changes the transverse scale and continuously deforms the local covariance distribution, but does not alter its global sphere covering. Accordingly, the reconstructed topological charge remains close to unity throughout the measurement propagation range $0 \leq z/f \leq 1$ (Fig. 5b).

Numerical simulations further examine the effects of attenuation and phase perturbations. Uniform loss rescales the covariance field while preserving its normalized direction, leaving the topological charge unchanged over the investigated transmission range (Fig. 5c). Selective attenuation of the OAM mode shifts the radial transition between the two poles but likewise preserves the unit charge (Fig. 5d). Under spatial phase noise, the mean charge remains close to unity over a broad range of σ_ϕ, with appreciable fluctuations appearing only for strong phase disorder (Fig. 5e). These results demonstrate that the topological charge is determined by the global organization of the covariance texture and remains stable under continuous spatial deformations.

Conclusion and discussion

We have introduced quantum squeezing skyrmions as a form of continuous-variable topology encoded in the covariance of a zero-mean quantum field. Unlike conventional optical skyrmions based on mean fields or first order coherence, these textures are carried by the anomalous pair correlation responsible for two-mode squeezing. The covariance simultaneously reveals the non-compact SU(1,1) geometry of squeezing through (K_0, K_1, K_2) and a compact S^2 mapping through the normalized vector (K_1, K_2, K_3). We generate these textures in an

OAM-pumped two-mode squeezed vacuum and reconstruct them using spatially resolved, phase-sensitive OPA tomography. Spatially resolved intensity oscillations provide the local covariance magnitude and phase, enabling the reconstruction of Wigner ellipses and topological charge of quantum squeezing skyrmions. Controlling the pair-phase offset and OAM winding produced Néel-type, Bloch type and anti-skyrmionic textures.

The same pair correlations that generate squeezing and entanglement therefore constitute the topology itself. The stability under propagation, attenuation and phase disorder shows that the charge characterizes the global organization. This robustness does not necessarily protect the squeezing or entanglement, but provides a complementary global descriptor of multimode quantum states under continuous deformations. The present realization considers a predominantly two-mode Gaussian state. Extending the approach to coherent superposition of multiple spatial modes and programmable multimode parametric interactions could enable skyrmion lattices and more general covariance topologies. Beyond the Gaussian regime, high-order correlations may support topological structures that cannot be captured by second moments alone. Spatially resolved parametric tomography could also be adapted to integrated nonlinear platforms and broadband multimode sources [42, 43], providing parallel characterization and control of structured quantum fluctuations.

More broadly, quantum squeezing skyrmions establish quantum correlations as physical carriers of optical topology. They connect the phase-space structure of continuous-variable quantum light with global geometry of skyrmionic fields, organizing quantum fluctuations into a controllable topological object. By combining locally useful squeezing correlations with globally structured information resilient to smooth deformations, these states may support spatially multiplexed quantum sensing and imaging with tailored noise suppression and robust mode tracking [44, 45]. They may also provide a framework for multimode quantum communication in which local continuous-variable information coexists with global topological state labels [46, 47].

References

[1] Skyrme, T. H. R. A non-linear field theory. *Proceedings of the Royal Society of London A* **260**, 127–138 (1961).

[2] Skyrme, T. H. R. A unified field theory of mesons and baryons. *Nuclear Physics* **31**, 556–569 (1962).

[3] Mühlbauer, S. *et al.* Skyrmion lattice in a chiral magnet. *Science* **323**, 915–919 (2009).

[4] Yu, X. Z. *et al.* Real-space observation of a two-dimensional skyrmion crystal. *Nature* **465**, 901–904 (2010).

[5] Ackerman, P. J., Trivedi, R. P., Senyuk, B., van de Lagemaat, J. & Smalyukh, I. I. Two-dimensional skyrmions and other solitonic structures in confinement-frustrated chiral nematics. *Physical Review E* **90**, 012505 (2014).

[6] Leslie, L. S., Hansen, A., Wright, K. C., Deutsch, B. M. & Bigelow, N. P. Creation and detection of skyrmions in a Bose–Einstein condensate. *Physical Review Letters* **103**, 250401 (2009).

[7] Choi, J.-y., Kwon, W. J. & Shin, Y.-i. Observation of topologically stable two-dimensional skyrmions in an antiferromagnetic spinor Bose–Einstein condensate. *Physical Review Letters* **108**, 035301 (2012).

[8] Das, S., Tang, Y. L., Hong, Z., Gonçalves, M. A. P. *et al.* Observation of room-temperature polar skyrmions. *Nature* **568**, 368–372 (2019).

[9] Ge, H. *et al.* Observation of acoustic skyrmions. *Physical Review Letters* **127**, 144502 (2021).

[10] Manton, N. & Sutcliffe, P. *Topological Solitons* (Cambridge University Press, Cambridge, 2004).

[11] Fert, A., Reyren, N. & Cros, V. Magnetic skyrmions: Advances in physics and potential applications. *Nature Reviews Materials* **2**, 17031 (2017).

[12] Jonietz, F. *et al.* Spin transfer torques in MnSi at ultralow current densities. *Science* **330**, 1648–1651 (2010).

[13] Romming, N. *et al.* Writing and deleting single magnetic skyrmions. *Science* **341**, 636–639 (2013).

[14] Woo, S. *et al.* Observation of room-temperature magnetic skyrmions and their current-driven dynamics in ultrathin metallic ferromagnets. *Nature Materials* **15**, 501–506 (2016).

[15] Forbes, A., de Oliveira, M. & Dennis, M. R. Structured light. *Nature Photonics* **15**, 253–262 (2021).

[16] Tsesses, S. *et al.* Optical skyrmion lattice in evanescent electromagnetic fields. *Science* **361**, 993–996 (2018).

[17] Du, L., Yang, A., Zayats, A. V. & Yuan, X. Deep-subwavelength features of photonic skyrmions in a confined electromagnetic field with orbital angular momentum. *Nature Physics* **15**, 650–654 (2019).

[18] Gao, S. *et al.* Paraxial skyrmionic beams. *Physical Review A* **102**, 053513 (2020).

[19] Gutiérrez-Cuevas, R. & Pisanty, E. Optical polarization skyrmionic fields in free space. *Journal of Optics* **23**, 024004 (2021).

[20] Sugic, D. *et al.* Particle-like topologies in light. *Nature Communications* **12**, 6785 (2021).

[21] Lin, M., Du, L. & Yuan, X. Photonic pseudospin skyrmion in momentum space. *IEEE Photonics Journal* **15**, 6500106 (2023).

[22] Teng, H. *et al.* Construction of optical spatiotemporal skyrmions. *Light: Science & Applications* **14**, 324 (2025).

[23] Wang, S. *et al.* Unveiling spin and Poynting dual textures of an optical skyrmionic tube in free space. *Physical Review Letters* **136**, 223803 (2026).

[24] Shen, Y. *et al.* Optical skyrmions and other topological quasiparticles of light. *Nature Photonics* **18**, 15–25 (2024).

[25] Ornelas, P., Nape, I., de Mello Koch, R. & Forbes, A. Non-local skyrmions as topologically resilient quantum entangled states of light. *Nature Photonics* **18**, 258–266 (2024).

[26] Ornelas, P., Nape, I., de Mello Koch, R. & Forbes, A. Topological rejection of noise by quantum skyrmions. *Nature Communications* **16**, 2934 (2025).

[27] de Mello Koch, R. *et al.* Revealing the topological nature of entangled orbital angular momentum states of light. *Nature Communications* **16**, 11095 (2025).

[28] Kleine, T. *et al.* Topological robustness of orbital angular momentum entanglement in stochastic channels. *Physical Review Letters* **137**, 050602 (2026).

[29] Ma, J. *et al.* Nanophotonic quantum skyrmions enabled by semiconductor cavity quantum electrodynamics. *Nature Physics* **21**, 1462–1468 (2025).

[30] Weedbrook, C. *et al.* Gaussian quantum information. *Reviews of Modern Physics* **84**, 621–669 (2012).

[31] Fabre, C. & Treps, N. Modes and states in quantum optics. *Reviews of Modern Physics* **92**, 035005 (2020).

[32] Yurke, B., McCall, S. L. & Klauder, J. R. SU(2) and SU(1,1) interferometers. *Physical Review A* **33**, 4033–4054 (1986).

[33] Shaked, Y. *et al.* Lifting the bandwidth limit of optical homodyne measurement with broadband parametric amplification. *Nature Communications* **9**, 609 (2018).

[34] Frascella, G., Zakharov, R. V., Tikhonova, O. V. & Chekhova, M. V. Multimode optical parametric amplification in the phase-sensitive regime. *Optics Letters* **46**, 2364–2367 (2021).

[35] Barakat, I. *et al.* Simultaneous measurement of multimode squeezing through multimode phase-sensitive amplification. *Optica Quantum* **3**, 36–44 (2025).

[36] Lyu, Z., Li, J., Li, P., Fang, Y. & Liu, Y. Topological harmonic generation of nonlinear optical skyrmions. *Ultrafast Science* **5**, 0104 (2025).

[37] Allen, L., Beijersbergen, M. W., Spreeuw, R. J. C. & Woerdman, J. P. Orbital angular momentum of light and the transformation of Laguerre–Gaussian laser modes. *Physical Review A* **45**, 8185–8189 (1992).

[38] Arlt, J., Dholakia, K., Allen, L. & Padgett, M. J. Parametric down-conversion for light beams possessing orbital angular momentum. *Physical Review A* **59**, 3950–3952 (1999).

[39] Arnaut, H. H. & Barbosa, G. A. Orbital and intrinsic angular momentum of single photons and entangled pairs of photons generated by parametric down-conversion. *Physical Review Letters* **85**, 286–289 (2000).

[40] Mair, A., Vaziri, A., Weihs, G. & Zeilinger, A. Entanglement of the orbital angular momentum states of photons. *Nature* **412**, 313–316 (2001).

[41] Franke-Arnold, S., Barnett, S. M., Padgett, M. J. & Allen, L. Two-photon entanglement of orbital angular momentum states. *Physical Review A* **65**, 033823 (2002).

[42] Knyazev, E., Spasibko, K. Y., Chekhova, M. V. & Khalili, F. Y. Quantum tomography enhanced through parametric amplification. *New Journal of Physics* **20**, 013005 (2018).

[43] Lenzini, F. *et al.* Integrated photonic platform for quantum information with continuous variables. *Science Advances* **4**, eaat9331 (2018).

[44] Brida, G., Genovese, M. & Ruo Berchera, I. Experimental realization of sub-shot-noise quantum imaging. *Nature Photonics* **4**, 227–230 (2010).

[45] Moreau, P.-A., Toninelli, E., Gregory, T. & Padgett, M. J. Imaging with quantum states of light. *Nature Reviews Physics* **1**, 367–380 (2019).

[46] Armstrong, S. *et al.* Programmable multimode quantum networks. *Nature Communications* **3**, 1026 (2012).

[47] Roslund, J., Medeiros de Araújo, R., Jiang, S., Fabre, C. & Treps, N. Wavelength-multiplexed quantum networks with ultrafast frequency combs. *Nature Photonics* **8**, 109–112 (2014).

Methods

Experiment. An amplified femtosecond ytterbium laser delivered 140-fs pulses centered at 1030 nm running with a repetition rate of 1 kHz and a maximum pulse energy of 2 mJ. The pump pulse energy incident on the optical setup was continuously adjusted using a half-wave plate followed by a wire-grid polarizer. The pump beam subsequently passed through a commercial spiral phase plate (SPP), which imprinted the desired orbital-angular momentum phase, and was focused by a lens with a focal length of 500 mm. Two 3-mm-thick β-barium borate (BBO) crystals configured for type-I phase matching were positioned on opposite sides of the beam focus, with a crystal-to-crystal separation of 60 cm. The first crystal (BBO 1) generated the two-mode squeezed vacuum (TMSV). The residual pump and the generated squeezed vacuum then propagated through a pair of oppositely oriented fused-silica wedges placed between the two BBO crystals. The wedge pair was mounted on a translation stage such that its transverse displacement varied the effective fused-silica thickness experienced by the optical fields. Owing to the material dispersion of fused silica, this displacement controlled the relative phase between the pump and TMSV $\Delta\varphi = \varphi_p - \varphi_s$. The pump and TMSV subsequently entered the second crystal (BBO 2), which operated as a phase-sensitive optical parametric (OPA). The amplification or deamplification of the TMSV was controlled by the pump-signal phase $\Delta\varphi$. After BBO 2, the residual 1030-nm pump was suppressed using a broadband optical filter centered at 2000 nm with a full width at half maximum (FWHM) of 500 nm. The TMSV was subsequently passed through a narrowband filter centered at 2050 nm with an FWHM of 20 nm. This narrowband filtering selected an effectively single spectral mode of the TMSV (see Extended Data Fig. 4). The filtered field was then collimated, and its transverse intensity distribution was recorded using a camera.

Quantum squeezing skyrmions. We first recall the coherence-matrix description of a conventional two-component optical field. Let $\hat{a}_j$ denote the annihilation operator of mode $j = 0, 1$, and define $N_j = \langle \hat{a}_j^\dagger \hat{a}_j \rangle$ and $C = \langle \hat{a}_0^\dagger \hat{a}_1 \rangle$. The normally ordered first-order coherence matrix is [48].

$$\Gamma = \begin{pmatrix} N_0 & C^* \\ C & N_1 \end{pmatrix} = \frac{1}{2} \left(S_0 \mathbb{I} + S_1 \sigma_x + S_2 \sigma_y + S_3 \sigma_z \right), \tag{11}$$

where $\sigma_{x,y,z}$ are the Pauli matrices and

$$S_0 = N_0 + N_1, \qquad S_1 = 2\,\mathrm{Re}\, C, \qquad S_2 = 2\,\mathrm{Im}\, C, \qquad S_3 = N_0 - N_1. \tag{12}$$

The normalized Stokes vector $\boldsymbol{s} = (S_1, S_2, S_3)/|(S_1, S_2, S_3)|$ lies on the compact Bloch sphere S^2. Conventional optical skyrmions are therefore maps from the transverse plane to S^2 encoded in first-order coherence. The squeezing texture considered here is instead encoded in the anomalous second-order coherence

$$M = \langle \hat{a}_0 \hat{a}_1 \rangle \,. \tag{13}$$

The corresponding symmetrically ordered Nambu covariance matrix is

$$\mathcal{G} = \begin{pmatrix} N_0 + \frac{1}{2} & M^* \\ M & N_1 + \frac{1}{2} \end{pmatrix} = \frac{1}{2} \left(K_0 \mathbb{I} + K_1 \sigma_x + K_2 \sigma_y + K_3 \sigma_z \right), \tag{14}$$

with $K_0 = N_0 + N_1 + 1, K_1 = 2\,\mathrm{Re}\, M, K_2 = 2\,\mathrm{Im}\, M$ and $K_3 = N_0 - N_1$. Here K_0 is the total symmetrized fluctuation, K_1 and K_2 are the two phase-orthogonal components of the pair coherence, and K_3 is the mode-population imbalance.

The two-mode SU(1, 1) generators are defined as

$$\hat{L}_1 = \frac{\hat{a}_0^\dagger \hat{a}_1^\dagger + \hat{a}_0 \hat{a}_1}{2}, \qquad \hat{L}_2 = \frac{\hat{a}_0 \hat{a}_1 - \hat{a}_0^\dagger \hat{a}_1^\dagger}{2i}, \qquad \hat{L}_3 = \frac{\hat{N}_0 + \hat{N}_1 + 1}{2}, \tag{15}$$

and obey $[\hat{L}_1, \hat{L}_2] = i\hat{L}_3, [\hat{L}_2, \hat{L}_3] = -i\hat{L}_1$ and $[\hat{L}_3, \hat{L}_1] = -i\hat{L}_2$. With the convention above, the covariance components are related to the generator expectation values by $(K_1, K_2, K_0) = 2\left(\langle \hat{L}_1 \rangle, \langle \hat{L}_2 \rangle, \langle \hat{L}_3 \rangle\right)$.

Thus, (K_0, K_1, K_2) carries the Lorentzian geometry of SU(1, 1), whereas K_3 is a conserved population-difference coordinate rather than an additional SU(1, 1) generator. For reference, the two-mode squeezed vacuum produced by the first parametric amplifier is written in our phase convention as $|\mathrm{TMSV}\rangle = \frac{1}{\cosh G_1} \sum_{n=0}^{\infty} \left(e^{i\phi_1} \tanh G_1\right)^n |n, n\rangle$, for which $N_0 = N_1 \equiv N = \sinh^2 G_1, M = \frac{1}{2} e^{i\phi_1} \sinh(2G_1)$ and $|M|^2 = N(N + 1)$. The four covariance components then reduce to $K_0 = \cosh(2G_1)$, $K_1 = \sinh(2G_1) \cos\phi_1$, $K_2 = \sinh(2G_1) \sin\phi_1$, and $K_3 = 0$, and consequently satisfy the hyperbolic constraint $K_0^2 - K_1^2 - K_2^2 = 1$. The ideal squeezing states therefore occupy the upper sheet of a two-sheet hyperboloid, the non-compact analogue of the Bloch sphere.

To introduce the spatial structure, the field is expanded in two orthonormal transverse modes $u_0(\boldsymbol{r})$ and $u_1(\boldsymbol{r})$,

$$\hat{b}(\boldsymbol{r}) = u_0(\boldsymbol{r}) \hat{a}_0 + u_1(\boldsymbol{r}) \hat{a}_1, \qquad \int u_i^*(\boldsymbol{r}) u_j(\boldsymbol{r})\, \mathrm{d}^2\boldsymbol{r} = \delta_{ij}. \tag{16}$$

The local component fields are $\hat{a}_j(\boldsymbol{r}) = u_j(\boldsymbol{r}) \hat{a}_j$, and their anomalous coherence is $M(\boldsymbol{r}) = \langle \hat{a}_0(\boldsymbol{r}) \hat{a}_1(\boldsymbol{r}) \rangle = u_0(\boldsymbol{r}) u_1(\boldsymbol{r}) M$. The compactified covariance texture is constructed from

$$\boldsymbol{d}(\boldsymbol{r}) = \begin{pmatrix} K_1(\boldsymbol{r}) \\ K_2(\boldsymbol{r}) \\ K_3(\boldsymbol{r}) \end{pmatrix} = \begin{pmatrix} 2\,\mathrm{Re}\, M(\boldsymbol{r}) \\ 2\,\mathrm{Im}\, M(\boldsymbol{r}) \\ N_0 |u_0(\boldsymbol{r})|^2 - N_1 |u_1(\boldsymbol{r})|^2 \end{pmatrix}, \qquad \boldsymbol{n}(\boldsymbol{r}) = \frac{\boldsymbol{d}(\boldsymbol{r})}{|\boldsymbol{d}(\boldsymbol{r})|}. \tag{17}$$

The pair (K_1, K_2) specifies the magnitude and phase of the local pair coherence, while K_3 specifies the local mode imbalance. The topological charge of the normalized covariance texture is

$$Q = \frac{1}{4\pi} \int \boldsymbol{n} \cdot (\partial_x \boldsymbol{n} \times \partial_y \boldsymbol{n})\, \mathrm{d}x\, \mathrm{d}y. \tag{18}$$

As a representative example, we take a fundamental Gaussian mode and an OAM mode with equal waists, $u_0(r, \varphi) = \mathcal{N}_0 \exp\left(-\frac{r^2}{w^2}\right)$ and $u_1(r, \varphi) = \mathcal{N}_1 \left(\frac{\sqrt{2} r}{w}\right)^{|\ell|} \exp\left(-\frac{r^2}{w^2}\right) e^{i\ell\varphi}$. Writing $\varphi_0 = \arg M$, the texture takes the axisymmetric form

$$\begin{aligned} K_1(r, \varphi) &= K_\perp(r) \cos(\ell\varphi + \varphi_0), \\ K_2(r, \varphi) &= K_\perp(r) \sin(\ell\varphi + \varphi_0), \qquad\qquad K_\perp(r) = 2|M|\, |u_0(r) u_1(r)|. \\ K_3(r) &= N_0 |u_0(r)|^2 - N_1 |u_1(r)|^2, \end{aligned} \tag{19}$$

For the balanced two-mode squeezed vacuum, $N_0 = N_1 = N$ and $|M|^2 = N(N + 1)$. The squared magnitude of the covariance vector is therefore

$$\begin{aligned} K_1^2 + K_2^2 + K_3^2 &= K_\perp^2 + K_3^2 \\ &= 4N(N + 1) |u_0|^2 |u_1|^2 + N^2 \left(|u_0|^2 - |u_1|^2\right)^2 \end{aligned}$$

$$= N^2\left(|u_0|^2+|u_1|^2\right)^2 + 4N|u_0|^2|u_1|^2. \tag{20}$$

In the large-photon-number limit, $N \gg 1$, this reduces to $K_1^2+K_2^2+K_3^2 \simeq N^2\left(|u_0|^2+|u_1|^2\right)^2$, or equivalently, $|\boldsymbol{K}(r)| \simeq N\left[|u_0(r)|^2+|u_1(r)|^2\right]$. Introducing $\beta(r)$ through $\cos\beta(r) = \frac{K_3(r)}{|\boldsymbol{K}(r)|}$, the normalized texture is

$$\boldsymbol{n}(r,\varphi) = \begin{pmatrix} \sin\beta(r)\cos(\ell\varphi+\varphi_0) \\ \sin\beta(r)\sin(\ell\varphi+\varphi_0) \\ \cos\beta(r) \end{pmatrix}. \tag{21}$$

Substitution into the topological-charge integral yields

$$Q = \frac{\ell}{2}\left[\cos\beta(0) - \cos\beta(\infty)\right]. \tag{22}$$

Because the OAM mode vanishes as $r^{|\ell|}$ at the origin, the Gaussian mode sets $\cos\beta(0) = 1$. For equal-waist modes, $|u_1|/|u_0| \propto r^{|\ell|}$, so the OAM component dominates in the large-radius limit and $\cos\beta(\infty) = -1$. The limiting direction remains well defined even though both amplitudes vanish, allowing the transverse plane to be compactified. Consequently,

$$Q = \ell. \tag{23}$$

Thus, the quantum squeezing skyrmion carries the topological charge $Q = \ell$, which remains invariant under continuous deformations that preserve the continuity and boundary conditions of the covariance texture.

Spatially resolved Gaussian-state reconstruction. We adopt the standard continuous-variable Gaussian-state formalism and quadrature conventions [30]. The canonical modal quadratures are defined as

$$\hat{x}_j = \frac{\hat{a}_j + \hat{a}_j^\dagger}{\sqrt{2}}, \qquad \hat{p}_j = \frac{\hat{a}_j - \hat{a}_j^\dagger}{i\sqrt{2}}, \tag{24}$$

with $[\hat{x}_j, \hat{p}_k] = i\delta_{jk}$ and vacuum variance $V_{\rm vac} = 1/2$. For the ordering $\hat{\boldsymbol{R}} = (\hat{x}_0, \hat{p}_0, \hat{x}_1, \hat{p}_1)^{\mathsf{T}}$, the covariance matrix is defined by $V_{mn} = \frac{1}{2}\left\langle \Delta\hat{R}_m\Delta\hat{R}_n + \Delta\hat{R}_n\Delta\hat{R}_m \right\rangle$. For the zero-mean states considered here, single-mode anomalous moments and phase-insensitive intermode coherence vanish, $\langle\hat{a}_0^2\rangle = \langle\hat{a}_1^2\rangle = 0$ and $\langle\hat{a}_0^\dagger\hat{a}_1\rangle = 0$.

The previously defined moments N_0, N_1, and $M = (K_1 + iK_2)/2$ then determine the complete two-mode covariance matrix,

$$V = \begin{pmatrix} N_0+\frac{1}{2} & 0 & \mathrm{Re}\,M & \mathrm{Im}\,M \\ 0 & N_0+\frac{1}{2} & \mathrm{Im}\,M & -\mathrm{Re}\,M \\ \mathrm{Re}\,M & \mathrm{Im}\,M & N_1+\frac{1}{2} & 0 \\ \mathrm{Im}\,M & -\mathrm{Re}\,M & 0 & N_1+\frac{1}{2} \end{pmatrix}. \tag{25}$$

For a Gaussian state, the first moments and covariance matrix provide a complete specification of the state and its Wigner distribution [49]. The corresponding joint two-mode Wigner distribution is

$$W(\boldsymbol{R}) = \frac{\exp\left[-\frac{1}{2}\boldsymbol{R}^{\mathsf{T}}V^{-1}\boldsymbol{R}\right]}{(2\pi)^2\sqrt{\det V}}. \tag{26}$$

To display the local Wigner ellipse, we define the normalized spatial superposition mode

$$\hat{A}(\boldsymbol{r}) = \frac{u_0(\boldsymbol{r})\hat{a}_0 + u_1(\boldsymbol{r})\hat{a}_1}{\sqrt{\mathcal{I}(\boldsymbol{r})}}, \qquad \mathcal{I}(\boldsymbol{r}) = |u_0(\boldsymbol{r})|^2 + |u_1(\boldsymbol{r})|^2, \tag{27}$$

which satisfies $[\hat{A}(\boldsymbol{r}), \hat{A}^\dagger(\boldsymbol{r})] = 1$ at each fixed $\boldsymbol{r}$. Its population and anomalous moment are

$$\begin{aligned} \bar{N}(\boldsymbol{r}) &= \langle\hat{A}^\dagger(\boldsymbol{r})\hat{A}(\boldsymbol{r})\rangle = \frac{|u_0(\boldsymbol{r})|^2N_0 + |u_1(\boldsymbol{r})|^2N_1}{\mathcal{I}(\boldsymbol{r})}, \\ \mathcal{M}(\boldsymbol{r}) &= \langle\hat{A}^2(\boldsymbol{r})\rangle = \frac{2M(\boldsymbol{r})}{\mathcal{I}(\boldsymbol{r})}. \end{aligned} \tag{28}$$

The local quadrature at phase θ is $\hat{X}_\theta(\boldsymbol{r}) = [e^{-i\theta}\hat{A}(\boldsymbol{r}) + e^{i\theta}\hat{A}^\dagger(\boldsymbol{r})]/\sqrt{2}$, with variance $V_\theta(\boldsymbol{r}) = \bar{N}(\boldsymbol{r}) + 1/2 + \mathrm{Re}[\mathcal{M}(\boldsymbol{r})e^{-2i\theta}]$. The principal variances and the squeezing angle are therefore

$$V_{\rm sq}(\boldsymbol{r}) = \bar{N}(\boldsymbol{r}) + \frac{1}{2} - |\mathcal{M}(\boldsymbol{r})|, \qquad V_{\rm asq}(\boldsymbol{r}) = \bar{N}(\boldsymbol{r}) + \frac{1}{2} + |\mathcal{M}(\boldsymbol{r})|, \tag{29}$$

$$\theta_{\mathrm{sq}}(\boldsymbol{r}) = \frac{\arg \mathcal{M}(\boldsymbol{r}) + \pi}{2} \pmod{\pi}. \tag{30}$$

The additional $\pi/2$ selects the minimum-variance axis for the sign convention used here; the unoriented principal axis is specified by $\arg \mathcal{M}/2$. With the rotated coordinates

$$\begin{pmatrix} X_{\mathrm{sq}} \\ P_{\mathrm{sq}} \end{pmatrix} = \begin{pmatrix} \cos\theta_{\mathrm{sq}} & \sin\theta_{\mathrm{sq}} \\ -\sin\theta_{\mathrm{sq}} & \cos\theta_{\mathrm{sq}} \end{pmatrix} \begin{pmatrix} X \\ P \end{pmatrix}, \tag{31}$$

the spatially resolved Wigner function takes the elliptical form

$$W_{\boldsymbol{r}}(X,P) = \frac{\exp\left[-\dfrac{X_{\mathrm{sq}}^2}{2V_{\mathrm{sq}}(\boldsymbol{r})} - \dfrac{P_{\mathrm{sq}}^2}{2V_{\mathrm{asq}}(\boldsymbol{r})}\right]}{2\pi\sqrt{V_{\mathrm{sq}}(\boldsymbol{r})V_{\mathrm{asq}}(\boldsymbol{r})}}. \tag{32}$$

The quadrature squeezing is determined by comparing the minimum variance with the vacuum variance V_{vac},

$$\mathcal{S}(\boldsymbol{r}) = -10\log_{10}\left[\frac{V_{\mathrm{sq}}(\boldsymbol{r})}{V_{\mathrm{vac}}}\right] \ \mathrm{dB}. \tag{33}$$

A positive value of $\mathcal{S}(\boldsymbol{r})$, equivalently $V_{\mathrm{sq}}(\boldsymbol{r}) < V_{\mathrm{vac}}$, signifies genuine sub-vacuum quadrature squeezing.

Spatial distribution of the second-order correlation We next derive the spatially resolved zero-delay second-order correlation of the Gaussian–OAM two-mode squeezed field. Using the local field operator $\hat{b}(\boldsymbol{r}) = u_0(\boldsymbol{r})\hat{a}_0 + u_1(\boldsymbol{r})\hat{a}_1$, the normalized zero-delay intensity correlation is defined as

$$g^{(2)}(\boldsymbol{r};0) = \frac{\left\langle \hat{b}^{\dagger 2}(\boldsymbol{r})\hat{b}^2(\boldsymbol{r})\right\rangle}{\left\langle \hat{b}^{\dagger}(\boldsymbol{r})\hat{b}(\boldsymbol{r})\right\rangle^2}. \tag{34}$$

For the zero-mean Gaussian state considered here, the first-order intermodal coherence vanishes. The local mean photon number is therefore

$$n_b(\boldsymbol{r}) = \left\langle \hat{b}^{\dagger}(\boldsymbol{r})\hat{b}(\boldsymbol{r})\right\rangle = N_0|u_0(\boldsymbol{r})|^2 + N_1|u_1(\boldsymbol{r})|^2. \tag{35}$$

Because the single-mode anomalous moments vanish, the local phase-sensitive moment is $M(\boldsymbol{r}) = \left\langle \hat{b}^2(\boldsymbol{r})\right\rangle = 2u_0(\boldsymbol{r})u_1(\boldsymbol{r})M$, where $M = \langle \hat{a}_0\hat{a}_1\rangle$ is the modal anomalous pair coherence introduced above. Applying Wick's theorem to a zero-mean Gaussian field gives $\left\langle \hat{b}^{\dagger 2}(\boldsymbol{r})\hat{b}^2(\boldsymbol{r})\right\rangle = 2n_b^2(\boldsymbol{r}) + |M(\boldsymbol{r})|^2$. Substitution into Eq. (34) yields the general spatial correlation profile

$$g^{(2)}(\boldsymbol{r};0) = 2 + \frac{4|u_0(\boldsymbol{r})|^2|u_1(\boldsymbol{r})|^2|M|^2}{\left[N_0|u_0(\boldsymbol{r})|^2 + N_1|u_1(\boldsymbol{r})|^2\right]^2}. \tag{36}$$

For an ideal two-mode squeezed vacuum, the two modes have equal mean populations $N_0 = N_1 = N$ and $|M|^2 = N(N+1)$. Equation (36) then reduces to

$$g^{(2)}(\boldsymbol{r};0) = 2 + 4\left(1 + \frac{1}{N}\right)\frac{|u_0(\boldsymbol{r})|^2|u_1(\boldsymbol{r})|^2}{\left[|u_0(\boldsymbol{r})|^2 + |u_1(\boldsymbol{r})|^2\right]^2}. \tag{37}$$

The spatial dependence is governed by the normalized overlap of the Gaussian and OAM modes. At the beam center the OAM mode vanishes, whereas toward the outer periphery the Gaussian mode becomes negligible. In either limit, the anomalous pair coherence is suppressed and the correlation approaches the thermal value $g^{(2)}(\boldsymbol{r};0) = 2$. The correlation reaches its maximum where the two local modal intensities are equal, $|u_0(\boldsymbol{r})|^2 = |u_1(\boldsymbol{r})|^2$. At these positions, the maximum zero-delay correlation is $g^{(2)}_{\max}(0) = 3 + \frac{1}{N}$, which approaches 3 in the large-photon-number limit $N \gg 1$. Consequently, the spatial correlation forms an annular enhancement around the region of strongest Gaussian–OAM modal overlap, as shown by the measurements in Fig. 3a–c and the numerical results in Extended Data Fig. 6.

Phase-sensitive optical parametric amplification for quantum tomography. The second parametric

amplifier, with gain G_2 and pump phase δ relative to the input pair coherence, implements the Bogoliubov transformation

$$\begin{aligned}\hat{a}_{0,\mathrm{out}}(\boldsymbol{r}) &= \cosh G_2\, u_0(\boldsymbol{r})\hat{a}_0 + e^{i\delta}\sinh G_2\, u_1^*(\boldsymbol{r})\hat{a}_1^\dagger,\\ \hat{a}_{1,\mathrm{out}}(\boldsymbol{r}) &= \cosh G_2\, u_1(\boldsymbol{r})\hat{a}_1 + e^{i\delta}\sinh G_2\, u_0^*(\boldsymbol{r})\hat{a}_0^\dagger.\end{aligned} \tag{38}$$

The spatial photon-number densities in the two output channels are

$$\begin{aligned}n_0(\boldsymbol{r}) &= N_0\cosh^2 G_2\,|u_0(\boldsymbol{r})|^2 + (N_1+1)\sinh^2 G_2\,|u_1(\boldsymbol{r})|^2 + \sinh(2G_2)\,\mathrm{Re}\left[e^{-i\delta}M(\boldsymbol{r})\right],\\ n_1(\boldsymbol{r}) &= N_1\cosh^2 G_2\,|u_1(\boldsymbol{r})|^2 + (N_0+1)\sinh^2 G_2\,|u_0(\boldsymbol{r})|^2 + \sinh(2G_2)\,\mathrm{Re}\left[e^{-i\delta}M(\boldsymbol{r})\right].\end{aligned} \tag{39}$$

Their sum is $n_{\mathrm{tot}}(\boldsymbol{r};\delta) = n_{\mathrm{p}}(\boldsymbol{r}) + 2\sinh(2G_2)\,\mathrm{Re}\left[e^{-i\delta}M(\boldsymbol{r})\right]$, where the phase-insensitive contribution is $n_{\mathrm{p}}(\boldsymbol{r}) = \left[N_0\cosh^2 G_2 + (N_0+1)\sinh^2 G_2\right]|u_0(\boldsymbol{r})|^2 + \left[N_1\cosh^2 G_2 + (N_1+1)\sinh^2 G_2\right]|u_1(\boldsymbol{r})|^2$.

Using the spatial covariance components defined above, the measured total intensity becomes

$$n_{\mathrm{tot}}(\boldsymbol{r};\delta) = n_{\mathrm{p}}(\boldsymbol{r}) + \sinh(2G_2)\left[K_1(\boldsymbol{r})\cos\delta + K_2(\boldsymbol{r})\sin\delta\right]. \tag{40}$$

The phase-insensitive contribution was obtained by averaging the measured intensity over the OPA pump phase $n_{\mathrm{p}}(\boldsymbol{r}) = \frac{1}{2\pi}\int_0^{2\pi} n_{\mathrm{tot}}(\boldsymbol{r};\delta)\,\mathrm{d}\delta$.

After subtracting the phase-insensitive contribution, the phase-dependent intensity at each transverse position was fitted to

$$n_{\mathrm{tot}}(\boldsymbol{r};\delta) - n_p(\boldsymbol{r}) = A_{\mathrm{OPA}}(\boldsymbol{r})\cos[\delta - \delta_M(\boldsymbol{r})], \tag{41}$$

where $A_{\mathrm{OPA}}(\boldsymbol{r})$ and $\delta_M(\boldsymbol{r})$ are the fitted oscillation amplitude and phase, respectively. Comparison with the covariance representation gives

$$A_{\mathrm{OPA}}(\boldsymbol{r}) = \sinh(2G_2)K_\perp(\boldsymbol{r}), \qquad \delta_M(\boldsymbol{r}) = \mathrm{atan2}[K_2(\boldsymbol{r}), K_1(\boldsymbol{r})] = \arg M(\boldsymbol{r}), \tag{42}$$

where $K_\perp(\boldsymbol{r}) = \sqrt{K_1^2(\boldsymbol{r}) + K_2^2(\boldsymbol{r})}$.

The transverse covariance components are therefore reconstructed as

$$\begin{aligned}K_1(\boldsymbol{r}) &= \frac{A_{\mathrm{OPA}}(\boldsymbol{r})}{\sinh(2G_2)}\cos\delta_M(\boldsymbol{r}),\\ K_2(\boldsymbol{r}) &= \frac{A_{\mathrm{OPA}}(\boldsymbol{r})}{\sinh(2G_2)}\sin\delta_M(\boldsymbol{r}).\end{aligned} \tag{43}$$

Equivalently, the fitted amplitude satisfies $A_{\mathrm{OPA}}(\boldsymbol{r}) = [n_{\max}(\boldsymbol{r}) - n_{\min}(\boldsymbol{r})]/2$.

Thus, the oscillation amplitude determines the magnitude of the local anomalous coherence, whereas its phase determines the local pair phase. Together with the independently measured population imbalance $K_3(\boldsymbol{r})$, these quantities determine the normalized squeezing texture $\boldsymbol{n}(\boldsymbol{r})$, its topological charge and the spatially resolved Wigner ellipses.

Methods references

[48] Mandel, L. & Wolf, E. *Optical Coherence and Quantum Optics* (Cambridge University Press, Cambridge, 1995).

[49] Adesso, G., Ragy, S. & Lee, A. R. Continuous variable quantum information: Gaussian states and beyond. *Open Systems & Information Dynamics* **21**, 1440001 (2014).

Author Contributions

Z.L. and J.L. designed and performed the experiments. Z.L. developed the theoretical framework, carried out the numerical simulations, analyzed the experimental data. Z.L. and Y.L. wrote the initial draft of the manuscript. Y.L. conceived and supervised the research. All authors discussed the results and contributed to reviewing and revising the manuscript.

Data availability

The data that support the plots within this paper and other findings of this study are available from the corresponding author upon reasonable request.

Code availability

The code used to produce the results is available from the corresponding author upon reasonable request.

Acknowledgements

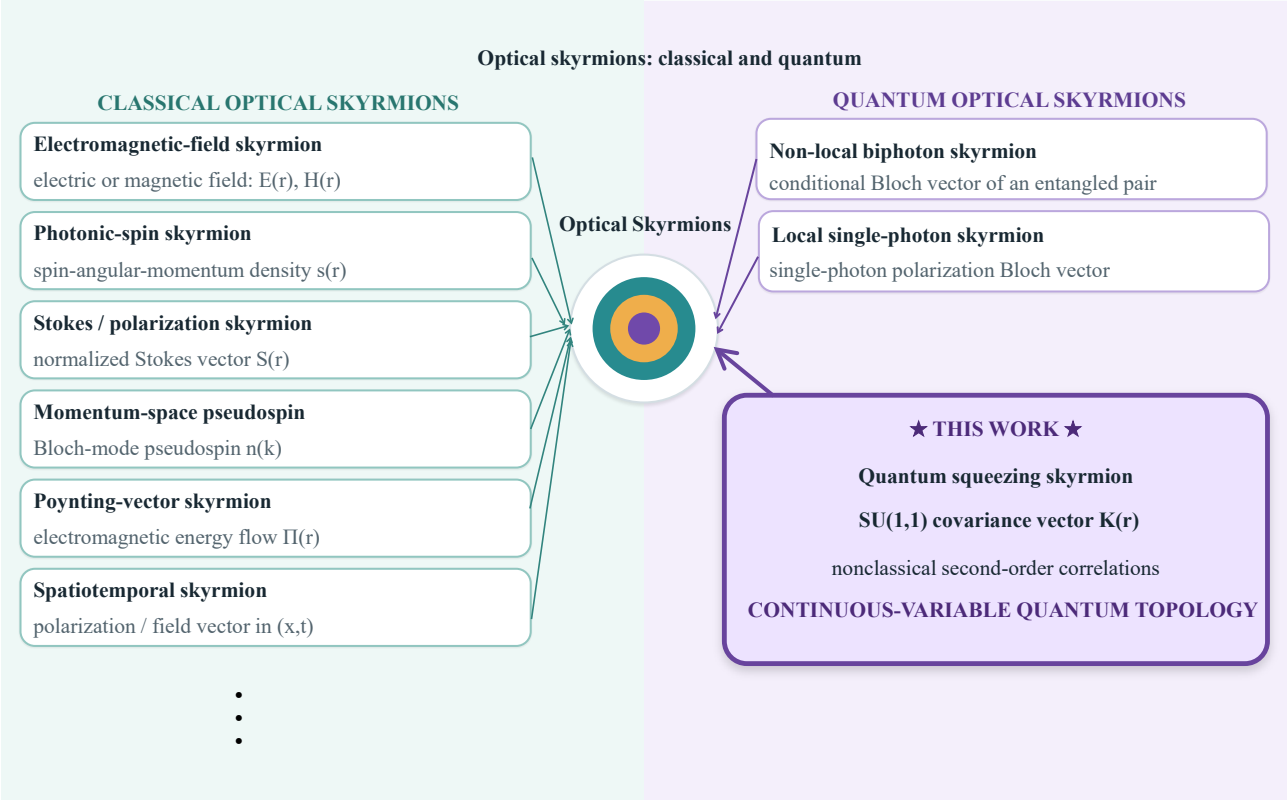
This project is supported by the National Key R&D Program (No. 2022YFA1604301), the Fundamental and Interdisciplinary Disciplines Breakthrough Plan of the Ministry of Education of China (No. JYB2025XDXM201), the Natural Science Foundation of China (No. 12334013) and Quantum Science and Technology-National Science and Technology Major Project (Grant No. 2025ZD0301000).

Additional information

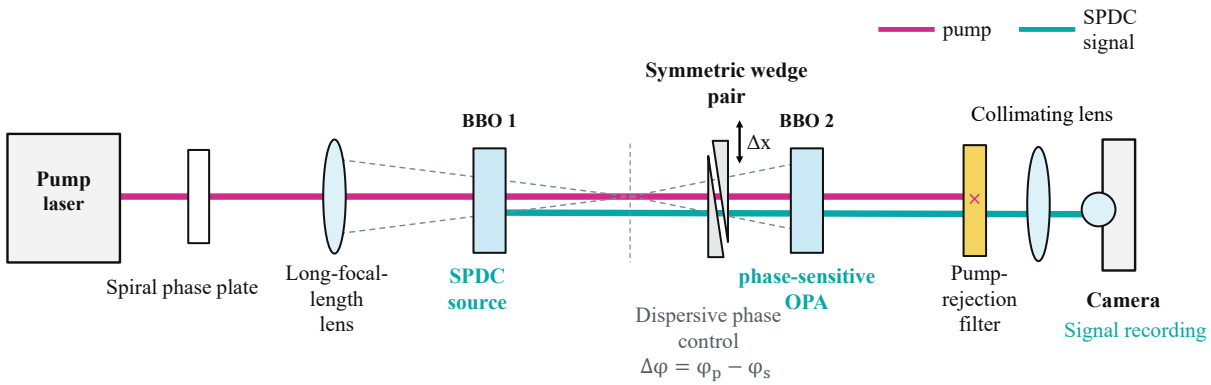
Correspondence and requests for materials should be addressed to Y. L.

Competing interests

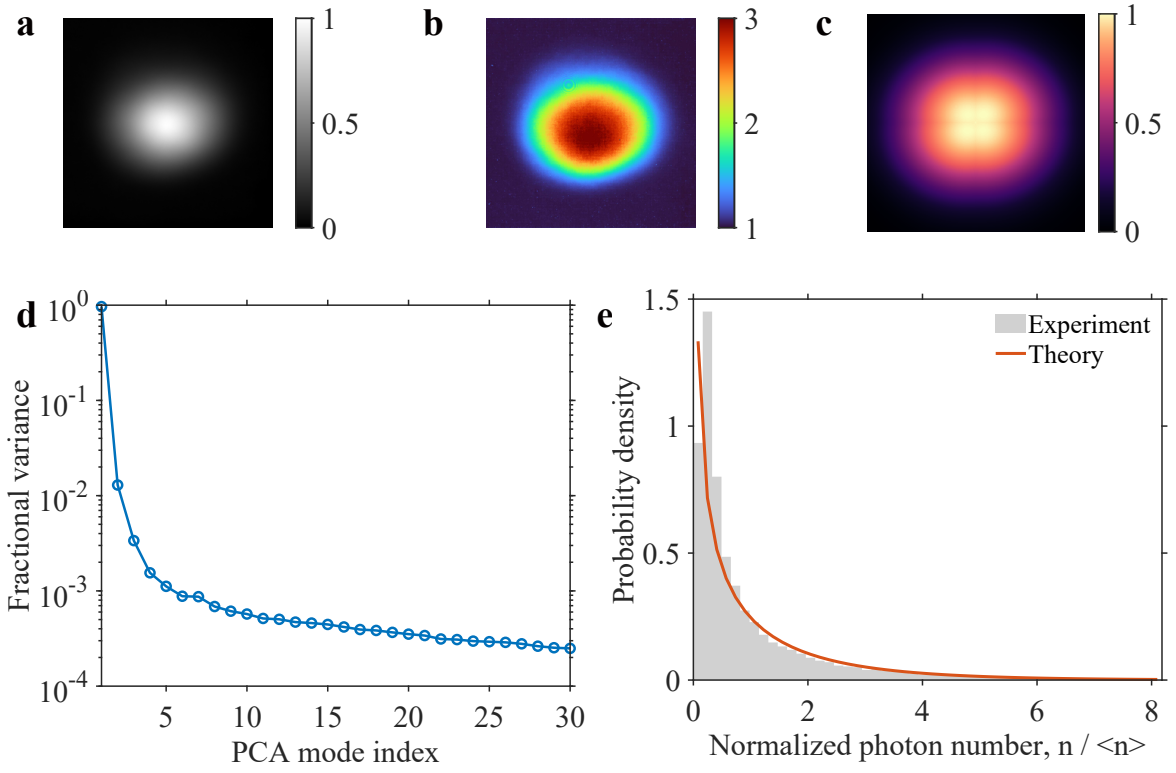
The authors declare no competing interests.



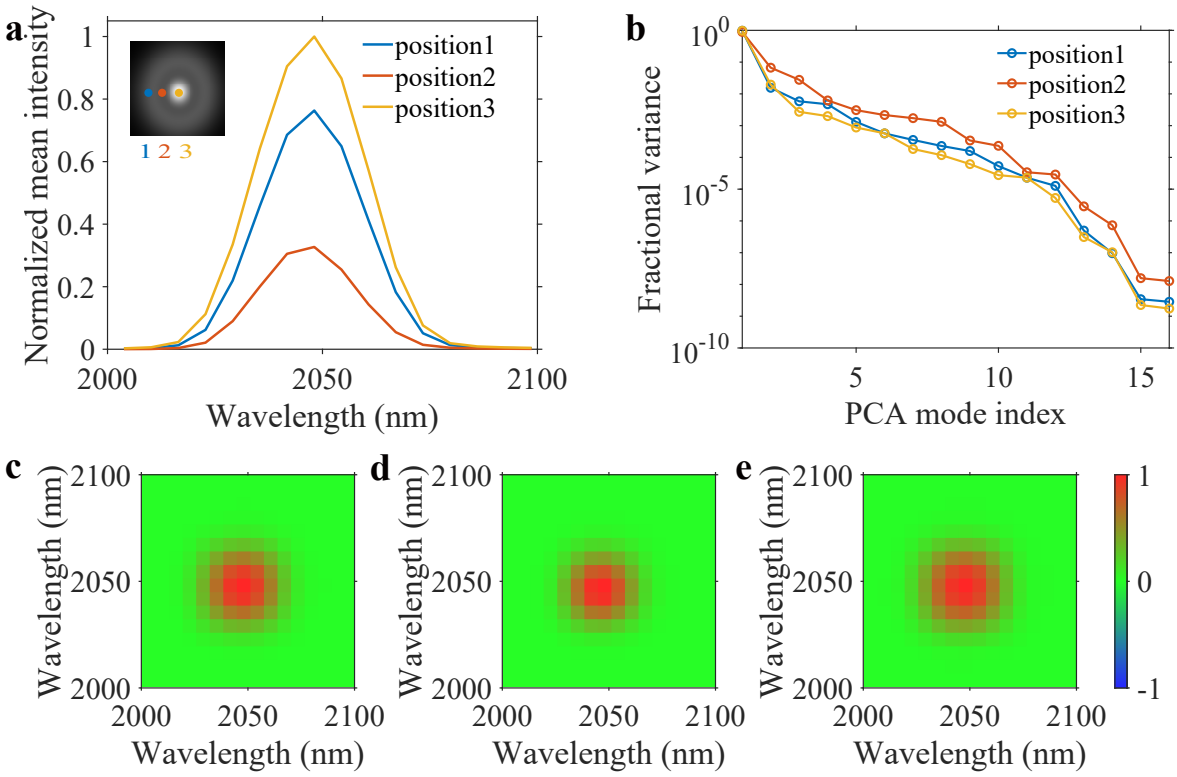
Extended Data Fig. 1 Classification of optical skyrmions according to their quantum character. The distinction between classical and quantum optical skyrmions is determined by whether the skyrmionic texture requires genuinely quantum properties of light. Classical optical skyrmions are fully described by classical field observables, including electromagnetic fields [16, 17], optical-spin densities and Poynting vectors [23], Stokes vectors [19], momentum-space pseudospins [21], and spatiotemporal fields [22]. Quantum optical skyrmions are instead encoded in observables of nonclassical photonic states, such as the conditional Bloch vector of an entangled photon pair [25] or the polarization state of a single photon [29]. The quantum squeezing skyrmion introduced here extends this concept to continuous-variable light: its texture is carried by the nonclassical second-order correlations of a two-mode squeezed vacuum and represented by a compactified covariance vector $\boldsymbol{K}(\boldsymbol{r})$.



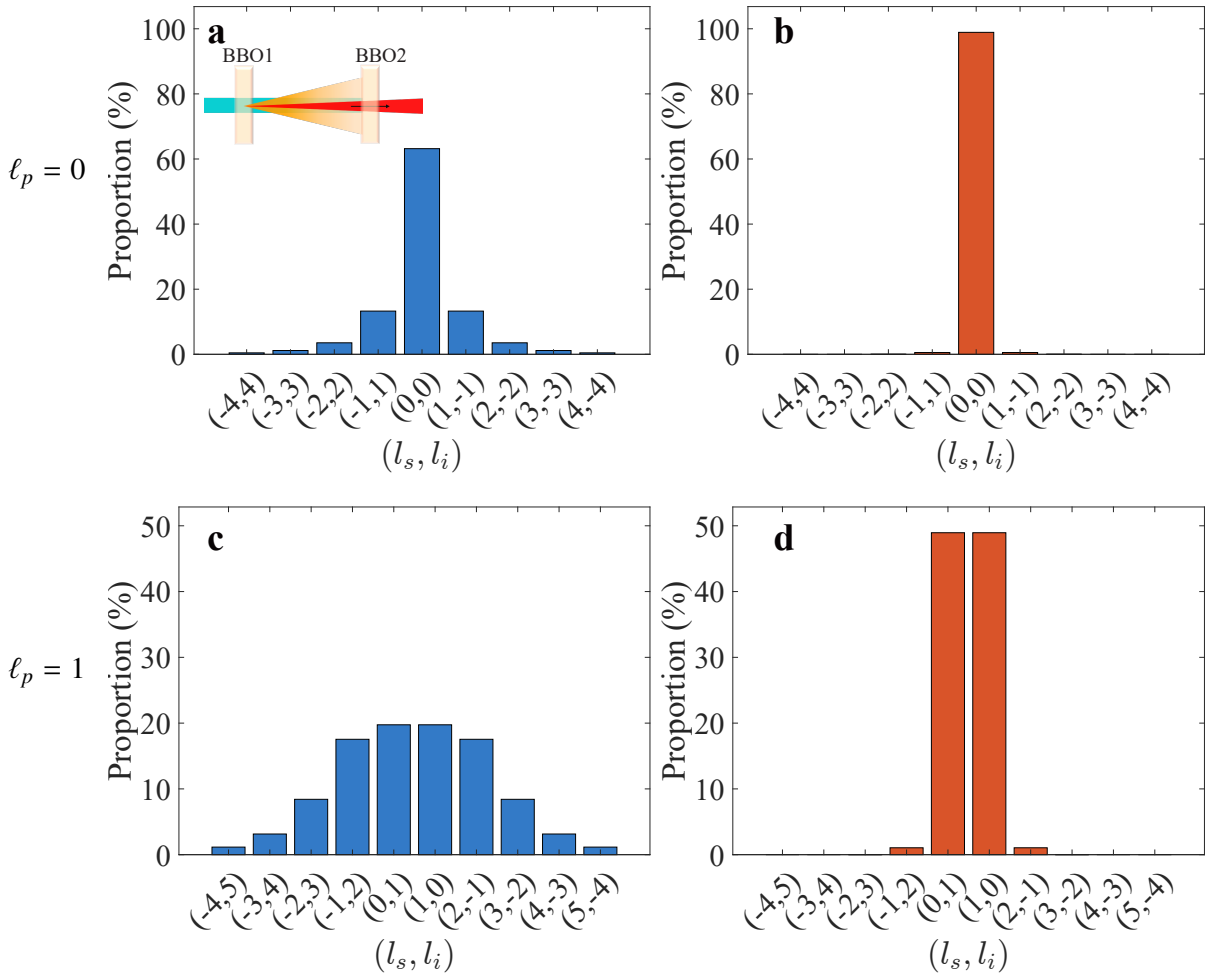
Extended Data Fig.2 Experimental setup. The pump beam passes through a spiral phase plate, which imprints the desired orbital angular momentum, and is subsequently focused by a long-focal-length lens. Two beta-barium borate (BBO) crystals are positioned on opposite sides of the focus. The first crystal (BBO 1) generates the spontaneous parametric down-conversion (SPDC) field. A symmetrically arranged wedge pair mounted on a translation stage controls the relative pump–signal phase, $\Delta\varphi = \varphi_{\mathrm{p}} - \varphi_{\mathrm{s}}$, through dispersion by varying the effective material thickness. The second crystal (BBO 2) acts as a phase-sensitive optical parametric amplifier (OPA). After amplification, the residual pump is removed by a pump-rejection filter, and the SPDC signal is collimated and recorded by a camera.



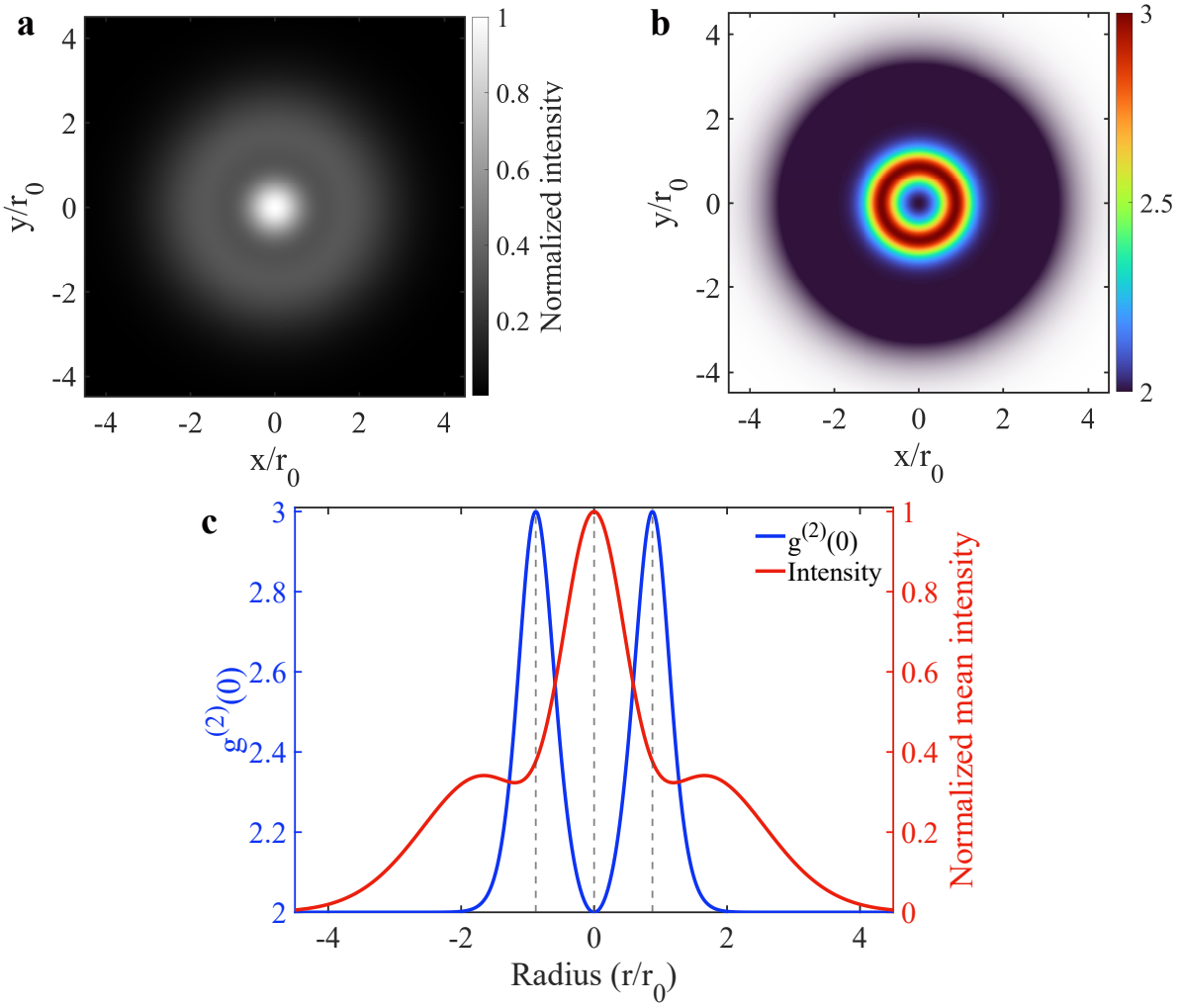
Extended Data Fig.3 Single-spatial-mode squeezed vacuum (SV) under an $\ell = 0$ pump. a, Normalized intensity distribution of the squeezed vacuum generated using a pump with zero OAM, $\ell_p = 0$. **b,** Measured spatial distribution of the second-order correlation function $g^{(2)}(0)$. **c,** Normalized spatial autocorrelation of the SV intensity distribution. **d,** Fractional variance carried by the principal-component analysis (PCA) modes as a function of the PCA mode index. The logarithmic vertical scale highlights the dominant contribution of the first spatial mode and the rapidly decreasing contributions of higher-order modes. The extracted effective spatial-mode number is $K_{\text{eff}} = 1.072$, confirming the near-single-spatial-mode character of the SV. **e,** Probability density of the normalized photon number $n/\langle n \rangle$. The gray histogram shows the experimental photon-number statistics, and the orange curve represents the corresponding theoretical results.



Extended Data Fig.4 Spectral single-mode character of the SV under an $\ell_p = 1$ pump. **a,** Normalized measured spectra at three representative transverse positions, as indicated in the inset. Owing to the type-I phase-matching configuration, the signal and idler are spectrally degenerate and exhibit overlapping spectra centered near the degenerate wavelength. The spectra measured at the three positions have the same spectral profiles, differing primarily in intensity. **b,** Fraction of the total variance contributed by each PCA mode for the three spatial positions. At all positions, the variance is strongly dominated by the first PCA mode, demonstrating the near-single-spectral-mode character of the SV. **c**–**e**, Normalized spectral covariance measured at position 1–3, respectively. The localized covariance, together with the dominant first PCA component, confirm the spectral single-mode character across the spatial profile.



Extended Data Fig.5 Selection of low-order OAM mode pairs by the second BBO crystal. a,b, Proportions of the signal–idler orbital-angular-momentum (OAM) mode pairs (ℓ_s, ℓ_i) for a Gaussian pump with $\ell_p = 0$, before (**a**) and after (**b**) the angular-mode selection imposed by BBO 2. The field generated by BBO 1 contains a broad distribution of OAM mode pairs satisfying $\ell_s + \ell_i = \ell_p$. Because BBO 2 predominantly accepts modes with small emission angles, the output is dominated by the $(\ell_s, \ell_i) = (0, 0)$ pair. **c,d**, Corresponding OAM-pair distributions for an OAM pump with $\ell_p = 1$. Before angular-mode selection, multiple mode pairs satisfying $\ell_s + \ell_i = 1$ contribute to the field (**c**). After BBO 2, the two lowest-order mode pairs, $(\ell_s, \ell_i) = (0, 1)$ and $(1, 0)$, become dominant with approximately equal proportions (**d**). The finite angular acceptance of BBO 2 therefore suppresses higher-order OAM components while preserving OAM conservation, thereby isolating the two-mode subspace required for preparing a high-purity quantum squeezing skyrmion.



Extended Data Fig.6 Numerical simulation of the intensity and second-order correlation of quantum squeezing skyrmions. a, Simulated phase-averaged mean-intensity distribution, normalized to its maximum value. The transverse coordinates are normalized by the reference radius r_0 used in Fig. 3. **b**, Corresponding spatial distribution of the zero-delay second-order correlation $g^{(2)}(\boldsymbol{r};0)$. At the beam centre, the OAM mode vanishes, whereas near the outer edge the Gaussian mode becomes negligible. In both regions, the local anomalous pair coherence is therefore suppressed, and the zero-delay correlation approaches the thermal value $g^{(2)}(\boldsymbol{r};0) = 2$. In the annular region where the Gaussian and OAM modes overlap, the phase-sensitive pair coherence is enhanced and $g^{(2)}(0)$ approaches 3. **c**, Radial profiles of $g^{(2)}(0)$ (blue, left axis) and the normalized mean intensity (red, right axis). These simulations provide the theoretical description of the measurements presented in Fig. 3a–c.

Supplementary Files

This is a list of supplementary files associated with this preprint. Click to download.

- supplement.pdf
- Q1.mp4
- gaussianmode.mp4